TAMPEREEN TEKNILLINEN YLIOPISTO
TAMPERE UNIVERSITY OF TECHNOLOGY

SALLA YLIPÄÄ

MONTE CARLO SIMULATIONS OF AN AXIAL POSITRON EMISSION TOMOGRAPHY DEMONSTRATOR

Master of Science Thesis

Examiners: Prof. Ulla Ruotsalainen
Prof. Jari Viik
M.Sc. Defne Us
Examiners and topic approved by Faculty Council of Computing and Electrical Engineering on January 14th 2015

TIIVISTELMÄ

TAMPEREEN TEKNILLINEN YLIOPISTO
Diplomi-insinöörin tutkinto
YLIPÄÄ, SALLA: Aksiaalisen positroniemissiotomografiprototyypin Monte Carlo simulaatiot
Diplomityö, 55 sivua
Huhtikuu 2015
Pääaine: Biolääketieteen instrumentointi
Tarkastajat: Prof. Ulla Ruotsalainen, Prof. Jari Viik, M.Sc. Defne Us
Avainsanat: Positroniemissiotomografia, PET, aksiaalinen PET, Monte Carlo simulaatiot, GATE, pituuskoordinaatin määritys, WLS liuska, suorituskyky

Aksiaalinen positroniemissiotomografi rakentuu skintillatiokristallien kerroksista jotka on asennettu laitteen pituusakselin suuntaisesti. Fotonien törmäyksien pituuskoordinaatit saadaan kohtisuoraan kristalleja vasten asetuista aallonpituusmuunninliuskojen riveistä. Tällä rakenteella on mahdollista kerätä tieto törmäyssyvyydestä, mikä poistaa parallaksivirheen ja näin mahdollistaa laitteen herkkyyden ja paikkaerottelukyvyn yhtäaikaisen kehittämisen.

Tässä opinnäytetyössä rakennettiin tietokonemalli aksiaalisesta positroniemissio-tomografiprototyypistä käyttäen simulaatiotyökalu GATEa. Malli perustuu AvanTomography-nimiseen prototyyppiin, jota kehitetään Tampereen teknillisessä yliopistossa, ja sen tarkoituksena on auttaa prototyypin suunnittelussa mahdollistamalla helppo ominaisuuksien tutkiminen ja testaus Monte Carlo simulaatioilla. Tämä opinnäytetyö sisältää mallin kehittämisen ja validoinnin, sekä suorituskykytestien ensimmäiset tulokset.

Kehitetty malli koostuu prototyypin geometriasta, johon kuuluu laitteen moduulien sisältämät skintillaatiokristallit ja aallonpituusmuunninliuskat, sekä signaalien lukemisesta ja elektronisesta prosessoinnista. Törmäyksien pituuskoordinaatti määritetään simuloimalla liuskojen vastetta. Koska GATE ei tue tämän kaltaista törmäyskoordinaattien määritystä, lisättiin tässä opinnäytetyössä GATEn ohjelmakoodiin uusi prosessointimoduuli. Uusi moduuli simuloi analyyttisesti skintillaatiofotonien kulkua ja jakaumaa kristalleissa ja aallonpituusmuunninliuskoissa, ja prosessoi liuskojen vasteen törmäysten pituuskoordinaateiksi. Lisäksi moduuli vastaa törmäyspulssien summauksesta sekä koordinaattien diskretoinnista.

Ensimmäiseksi malli validoitiin tarkastelemalla törmäysten määrää ja energiaspektriä, ja tutkimalla pituuskoordinaattien määräytymistä. Seuraavaksi sarja simulaatioita ajettiin selvittämään prototyypin suorituskyky. Laitteen herkkyys testattiin kolmesta eri moduulikonfiguraatioista, lisäksi testattiin herkkyyden kasvu moduulikerrosten lisäyksen funktiona. Tämän jälkeen selvitettiin sironnan määrä ja kohinaa vastaava lukemataajuus rotan kokoiselle fantomille. Tulokset osoittavat, että rakennettua mallia voidaan käyttää aksiaalisen positroniemissiotomografian toiminnan simulointiin, ja että sen avulla voidaan selvittää kokonaisen laitteen suorituskyky, edellämainittujen ominaisuuksien lisäksi myös erottelukyky ja kuvanlaatu. Koska muutoksia on helpompi tehdä tietokonemalliin kuin oikeaan prototyyppiin, on tässä opinnäytetyössä rakennettu malli hyvä työkalu suunniteltujen muutoksien testaamiseen ennen niiden toteutusta.

ABSTRACT

TAMPERE UNIVERSITY OF TECHNOLOGY
Master's Degree Programme in Electrical Engineering
YLIPÄÄ, SALLA: Monte Carlo simulations of an axial positron emission tomography demonstrator
Master of Science Thesis, 55 pages
April 2015
Major: Medical instrumentation
Examiners: Prof. Ulla Ruotsalainen, Prof. Jari Viik, M.Sc Defne Us
Keywords: Positron emission tomography, PET, axial PET, Monte Carlo simulations, GATE, axial coordinate determination, WLS strip, performance

Axial positron emission tomography (PET) scanners are composed of layers of scintillating crystals aligned with the main axis of the scanner. The axial coordinates of photon interaction events are obtained using a matrix of wavelength shifting strips placed orthogonally to the crystals. This construction allows acquiring depth of interaction information of the events, which removes the parallax error enabling simultaneous improvement of the scanners' sensitivity and spatial resolution.

In this thesis a computer model of the axial PET demonstrator called AvanTomography was built using GATE simulation toolkit. The model is based on the real demonstrator that is being constructed at Tampere University of Technology; the purpose of the model is to help in designing the demonstrator by enabling easy testing and characterisation using Monte Carlo simulations. This thesis describes the construction and validation of the model, and the initial results of performance testing.

The model includes the demonstrator's modular structure with scintillating crystals and wavelength shifting strips, signal read out and processing electronics. The axial coordinates of events are determined by simulating event positioning with the strips. As GATE does not currently support such novel event positioning, a new processing module was written into GATE source code as part of this thesis work. This new module simulates analytically the transport and distribution of scintillation photons in the scintillating crystals and wavelength shifting strips, and processes the signals in order to determine the axial coordinate of the events. In addition, the module handles pulse adding and discretisation of event radial and tangential coordinates.

The built model was then used to run simulations to study the model and the demonstrator system. Firstly, the model was validated for produced energy spectra, event rates, and axial coordinate determination. Scanner constructions having 2, 4 and 8 modules were tested for sensitivity, as well as the increase of sensitivity when radial layers of modules are added. Then scatter fraction and noise equivalent count rate were simulated using a rat sized phantom. The results show that the model can be used in simulating the functionality of an axial PET scanner, and could in future be used to determine the performance, including spatial resolution and image quality, of a full-scale scanner. As it is easier to make changes to the model than the real scanner, running simulations with the constructed model is an efficient method for testing planned changes before implementation.

PREFACE

This thesis work was done in the Methods and Models for Biological Signals and Images research group at the Department of Signal Processing, Tampere University of Technology, Finland.

Firstly I would like to thank my supervisors Prof. Ulla Ruotsalainen, Prof. Jari Viik and MSc. Defne Us for this opportunity to work on a subject that has been demanding but at the same time so rewarding.

Secondly I would like to express my gratitude to my parents, Tarja Ylipää and Kari Ylipää, for always believing in me, and to my brother Antti Ylipää for going first. Especially I would like to thank Mikko Vartiala for his support and encouragement.

Tampere, March 2015
Salla Ylipää

CONTENTS

LIST OF SYMBOLS AND ABBREVIATIONS

α, θ	Angle
A	Signal amplitude, or radioactivity
β^+	Positron
β^-	Electron
γ	Gamma photon
C	Count (coincidence) rate
C_T	True count rate
C_S	Scattered count rate
C_R	Random count rate
cps	Counts per second
I	Intensity
μ	Attenuation coefficient
ν	Neutrino
n	Index of refraction
R_E	Energy resolution
R_S	Spatial resolution
R_T	Temporal resolution
σ	Standard deviation
S	Sensitivity
x, y, z	Coordinates in Cartesian system
2D	2-dimensional
3D	3-dimensional
APD	Avalanche photodiode
AX-PET	Axial positron emission tomography
BGO	Bismuth germanite
CDF	Cumulative distribution function
CT	Computed tomography
FDG	Fluorodeoxyglucose
FOV	Field of view
FWHM	Full width at half maximum
FWTM	Full width at tenth maximum
GATE	Geant4 application for emission tomography

LOR	Line of response
LYSO	Lutetium yttrium oxyorthosilicate
MPPC	Multi-pixel photon counter
NECR	Noise equivalent count rate
NEMA	National Electrical Manufacturers Association
PDF	Probability density function
PET	Positron emission tomography
PMT	Photomultiplier tube
RNG	Random number generator
SF	Scatter fraction
SPECT	Single photon emission tomography
WLS	Wavelength shifting
YAP	Yttrium aluminium perovskite

1 INTRODUCTION

The rapid development of medical imaging techniques in the 20th century is due to the discoveries of x-rays, radioactivity and nuclear magnetic resonance. While the structural imaging methods such as x-ray planar and computed tomographic (CT) imaging and magnetic resonance imaging (MRI) produce detailed images of the composition of biological tissues, there is also a need to image their functionality. Functional imaging makes it possible to image functions such as tissue sugar or oxygen uptake, blood flow and receptor densities. Modalities of functional imaging are, for example, the two nuclear imaging methods, single-photon emission tomography (SPECT) and positron emission tomography (PET); and functional MRI (fMRI).

The concept of PET was introduced already in the 1950s, and the development of the first PET scanner began in the 1970s by M.E. Phelps and colleagues [1]. It was made possible by the invention of radiopharmaceuticals, especially the ^{18}F -labelled glucose analogue fluorodeoxyglucose FDG [2], and tomographic image reconstruction. Since the early days, PET scanners have been greatly improved in terms of sensitivity, spatial resolution and scanning speed. PET imaging is now an important tool in assessing the patient's state in many clinical conditions including different types of cancer, and circulatory and neurological disorders [3], and it is also used in research including preclinical studies for drug development.

Development of PET scanners continues in order to achieve scanners with increased performance in terms of sensitivity, spatial resolution and count rate. While modern PET scanners already have a reasonably good performance, they still suffer from an effect called the parallax error that reduces spatial resolution at the peripheries of the field of view, which is caused by uncertainty of the depth of interaction (DOI). The parallax error is even amplified for scanners with higher sensitivity as there is an inherent trade-off between the two important characteristics, and smaller preclinical and organ dedicated (e.g. brain) PET scanners suffer even more from the trade-off than large full-body scanners. Modern scanners collect depth of interaction information by using layered radiation detectors which allows increasing the length of the detectors and thus the sensitivity without an increased parallax [4]. A novel approach to collect DOI information is to arrange the detectors in axial orientation and read the axial coordinate of hits with wavelength shifting strips, which enables recording a uniform spatial resolution over the whole field of view, while at the same time improving sensitivity [5]. This new construction is implemented in the AvanTomography PET demonstrator, aiming to achieve

a small and versatile scanner. The project is being conducted at Tampere University of Technology, Department of Signal Processing.

The aim of this thesis is to build a computer model of the AvanTomography demonstrator to be used in simulating the scanner's performance. The simulations to be run with the model use stochastic Monte Carlo method that is essential in simulating phenomena with random nature, as is the physics involved in PET imaging. Using Monte Carlo simulations it is possible to discern different factors of the structure and data processing that affect the scanner's performance; they allow testing planned adjustments before costly assembly and can be used to predict the best approach.

Using the model of AvanTomography demonstrator it is possible to simulate different scanner configurations and their effect to the performance of the system, helping in the design process of the demonstrator. The model allows studying characteristics such as sensitivity, spatial resolution, scatter fraction and count rate. The plan for this thesis project is to build the model and analyse the results concerning count rates and energy response and axial coordinate determination, and to run simulations to determine the sensitivity, scatter fraction and noise equivalent count rate of the demonstrator.

This thesis begins with a description of theory of positron emission tomography including the physical principle, operation and performance in Chapter 2. It is followed by a short theoretical consideration of Monte Carlo methods and descriptions of the used simulation tools in Chapter 3. Chapter 4 contains the details of the model with geometry, materials, event coordinate determination and other parameters, while the simulation set-ups are found in Chapter 5. The results are presented and analysed in Chapter 6, and the work is concluded finally in Chapter 7.

2 POSITRON EMISSION TOMOGRAPHY

Positron emission tomography (PET) is a functional *in vivo* imaging method. PET imaging measures the concentration and distribution of radiotracers, molecules labelled with positron emitting isotopes (e.g. ^{15}O, ^{18}F or ^{11}C), injected to the patient. The radiotracer concentration is imaged by detecting a pair of photons that result from annihilation of the emitted positron, with a ring of detectors. Using tomographic image reconstruction, a 3D image is constructed from the data of detected photons. Figure 2.1 shows the process of a PET scan from positron decay to reconstructed image. The power of PET imaging lies in the wide range of potential radiotracers; with different types of ligands it is possible to study functions ranging from blood flow to sugar metabolism to the amounts of specific receptor proteins. The most important clinical applications of PET are oncology, cardiology, and neurology, where it is used to diagnose, assess and follow the stage of the disease [3]. Majority of studies are currently conducted using a sugar analogue radiotracer, [^{18}F]-FDG, which is especially useful in revealing sites of high metabolism, such as malignant tumours. Examples of other commonly used tracers are [^{11}C]-methionine for amino-acid transport studies, [^{15}O]-oxygen for oxygen utilization studies, and [^{18}F]-F-DOPA for dopamine synthesis studies [6].

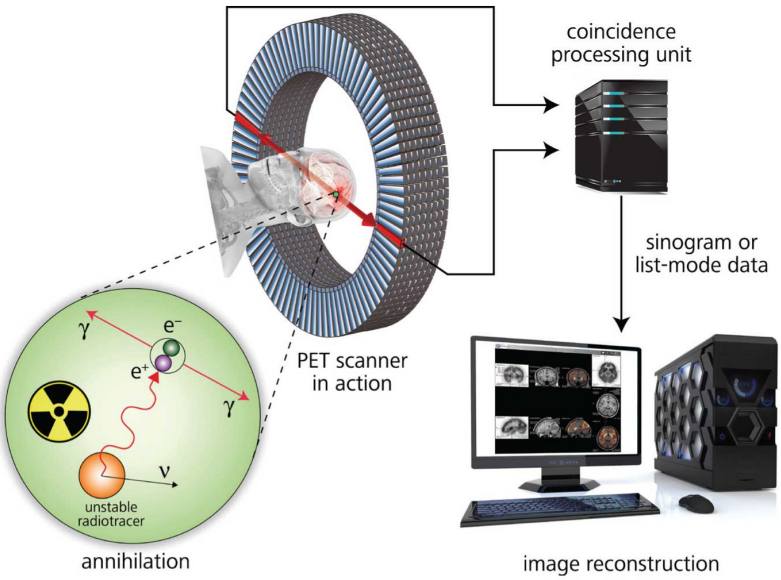

Figure 2.1: The principle of a PET scan. The gamma photons produced by positron decay are detected in the ring of the scanner and processed to form a tomographic image of the subject. [7]

2.1 PET basics

In this chapter the physical principle and instrumentation of positron emission tomography are explained. These are followed by a description of image construction and the performance characteristics associated with PET imaging.

2.1.1 PET physics

PET is based on detecting positron decay, also referred to as beta plus (β^+) decay, of a radioactive labelling isotope. Positron decay can happen in unstable isotopes rich with protons. In positron decay a proton (P) in the nucleus of an atom converts into a neutron (N), a positron (β^+) and a neutrino (v):

$$P \rightarrow N + \beta^+ + v \tag{2.1}$$

This process decreases the atomic number of the decaying element while the mass number is conserved. The energy released during the process is shared with the nucleus, the positron and the neutrino, and the positron and the neutrino are ejected from the nucleus. The total released energy E_{max} depends on the difference in the atomic masses of the parent and daughter atoms. A part of this total energy, ranging from 0 to E_{max}, is given to the positron as kinetic energy. The rate of decay, activity, of a radioactive isotope decreases exponentially, determined by the half-life of the isotope in question.

The positron ejected by the β^+ decay has a very short lifetime in matter. It loses kinetic energy in inelastic interactions with electrons, and when most of the energy is lost, the positron collides with an electron (β^-) and they annihilate:

$$\beta^- + \beta^+ = 2\gamma \tag{2.2}$$

Because the energy and the momentum of the annihilating particles must be conserved, two gamma-range photons (γ) are simultaneously emitted in opposite directions, each photon having 511 keV of energy. Figure 2.2 shows a schematic of positron decay and annihilation processes. The high energy of the photons means that they have a high probability of escaping the body without interactions, and thus they can be detected by the scanner. As the angle of the gamma photons is known to be ~180 degrees, the point of annihilation is along the line connecting the positions where the photons interact with the scanner.

The gamma photons from an annihilation event interact with matter largely by two mechanisms: photoelectric effect and Compton scattering. In photoelectric effect the photon gives all its energy to an electron located in an inner shell of an atom. The electron is ejected from the atom with the kinetic energy left after breaking the bond between the electron and the nucleus. An electron from the upper shell then drops to fill the vacancy on the inner shell, and a characteristic x-ray or an Auger electron is emitted. The probability of photoelectric effect increases with lower photon energies and higher atomic number of the matter.

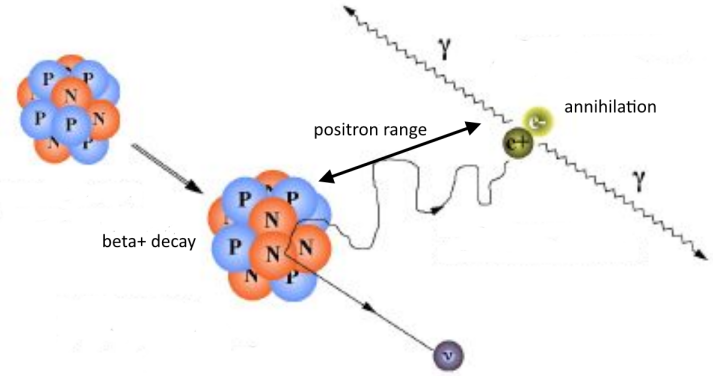

Figure 2.2: A proton of an unstable nucleus decays into a neutron, emitting a neutrino and a positron. The positron annihilates with an electron, resulting in two 511 keV photons travelling in opposite directions. Adapted from [8].

In Compton scattering the gamma transfers a part of its energy to an outer shell electron ejecting it. During the process the incident gamma photon changes direction, and the scattered photon may then undergo another scattering event, or be absorbed by photoelectric effect. The probability of Compton scattering increases with higher photon energy.

Attenuation, or energy transfer from particle to matter, of gamma photons constitute of the two processes described above. During an imaging session, attenuation happens in the patient as well as in the detector, the first of which has to be corrected for, while the second is essential for detecting the photons. The attenuation in material is described with equation:

$$I_x = I_0 e^{-\mu x} \tag{2.3}$$

Here I_x is the intensity of radiation at distance x in the material that depends on the initial intensity I_0, and two parameters; the distance and the linear attenuation coefficient μ that depends on the atomic number and density of the material and the energy of the radiation. [9] The detector material's capacity to attenuate photons, i.e. its stopping power, is an important characteristic of a PET scanner.

2.1.2 PET scanners

A conventional PET scanner comprises of several detector components assembled as rings to make a tubular scanner. The sensitive elements of the scanner are solid scintillators, also referred to as scintillating crystals, that exhibit luminescence. The crystals are read with photon detectors that produce a signal which is fed to a processing circuit.

The detection with scintillating crystals is based on absorption of the high energy photons that excite the crystal material. After a short delay, the material relaxes releasing photons on a shifted wavelength at visible light spectrum. The main characteristics of scintillating crystals are:

- Stopping power for 511 keV photons,
- scintillation decay time,
- light output and
- energy resolution.

The stopping power, which is the mean distance a photon travels before it stops, depends on the crystal's attenuation coefficient. The stopping power gives the detector's efficiency on detecting photons, which means that with a higher stopping power the thickness of the detector can be reduced while still detecting a reasonable portion of photons passing the detector. The scintillation decay time is the delay between the moment of an interaction and the emission of light, as the interacting atom is first excited to a higher energy level and after a certain delay returns to the ground state. The light output is the number of scintillation photons emitted per keV of incident photon. A higher light output leads to a better energy resolution, the ability to discriminate the incident photon's energy. Examples of detector materials used in PET scanners are BGO ($Bi_4Ge_3O_{12}$, widely used in commercial scanners), LSO (Lu_2SiO_5, used increasingly), GSO (Gd_2SiO_5), YAP ($YalO_3$) and BaF_2. [9]

The photon detectors used in PET can be either photo-multiplier tubes or semiconductor photodiodes. Photomultiplier tubes are vacuum glass tubes that have a photocathode, a series of dynodes and an anode. A scintillation photon reaching the photocathode liberates an electron with a 15 to 25 % chance, which is then accelerated through the PMT. As electrons hit the dynodes, more electrons are liberated, and a PMT thus has a gain in the order of $10^{6.}$. A downside of PMTs is that they are quite big: 1 to 5 cm in diameter.

Semiconductor photodiodes are made of a piece of silicon which is doped with impurities. A scintillation photon has a 60 to 80 % chance to liberate an electron from the silicon structure, and the electron and the hole then drift to the anode and cathode, respectively, in the applied electric field. Photodiodes have no internal gain which makes them unreliable in PET, but the efficiency is better than in PMTs. An improvement to the old photodiodes is the avalanche photodiode (APD) that has a much stronger electric field so that electrons gain more energy and have a chance to liberate consequent electrons. The gain of APDs is in the range of 10^2 to 10^3 which makes their performance competitive. APDs can be manufactured in various sizes which makes them flexible to use in different readout schemes. [10]

2.1.3 Image construction

The imaging process with a PET system involves detecting at the same time instant the two annihilation photons that hit the detector at opposite sides of the ring. The event of detecting a photon is referred as a *single* event, and two singles detected at the same time are connected to make a *coincidence* event. From the position information on the two singles, it is possible to know the line of response (LOR), along which the annihila-

tion occurred, and this information is collected to form projections of the imaged object. In a ring scanner, the possible LORs connected to one detector element form a fan in the transverse plane, defined by the acceptance angle (Figure 2.3). The fans of LORs for all the detectors outline the field of view (FOV), so that a larger angle of acceptance creates a larger FOV.

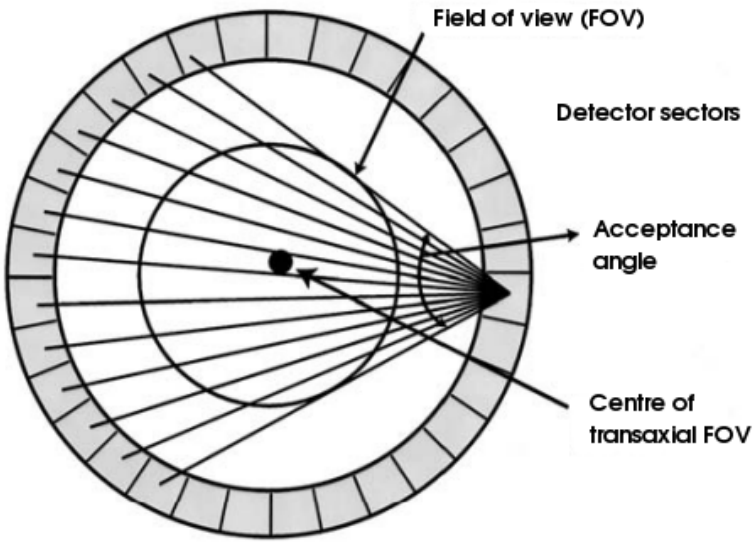

Figure 2.3 In the transverse plane, the possible LORs connected to a detector element on the right side of the scanner form a fan. The minimum sector difference (here 10) defines the acceptance angle. The fans for all detectors together define the FOV. Adapted from [9].

Clinical PET scanners often comprise of several consecutive detector rings that form planes along the z-axis. It is thus possible that a pair of photons hit detectors in different rings. The possibility can be handled in two ways: 2D and 3D modes. In 2D mode there are collimator septa between the scanner rings that prevent most cross-plane hits, therefore only the coincidences in the transverse plane are accepted. In 3D mode there is no septa and all cross-plane coincidences are accepted. The 3D mode has several times higher sensitivity, i.e. more coincidences are detected than in 2D mode, however more memory is needed to store the coincidence information and the quality of the image may degrade due to scattered and random coincidences (see Chapter 2.1.4). [9]

The coincidences can be stored in two different procedures: *list mode* and *histogram* mode. In list mode each coincidence event is written into a file, storing information on the locations and energies of the two single events and the time stamp of the interactions. List mode is flexible as it enables sorting events by detection time after acquisition, enabling further processing. Instead of storing coincidences, another option is to store the singles and form the coincidences from the list mode data as offline processing. In histogram mode a memory location is allocated for every possible LOR, and for each event seen in a certain LOR, the memory location is incremented. Histogram

data is presented as a 2D image, sinogram, composed of sine waves representing the imaged object. Histogram mode is usually more efficient way of storing data that the list mode, but also less flexible.

Another means of getting information on the location of the annihilation besides projections is measuring the *time of flight* (TOF) of the two coincident photons. From the difference in the detection times of the photons it is possible to calculate the point of origin, given that both photons travel at the speed of light and the distance between detection points is known. TOF information can be used to improve the signal to noise ratio of images, especially in large diameter full body scanners, but it requires high temporal resolution from the system.

2.1.4 Coincidence detection

PET scanners detect the two gamma photons travelling in opposing directions, and combines these into coincidence events (also known as prompt counts, or counts). The coincidence processing is done by applying a coincidence time window, usually in the range of 4 to 18 ns, either to detected singles (online processing), or to a list of stored singles (offline processing). If two singles in different sectors of the scanner within the time window are found, a coincidence is formed. It is then possible to find the line of response from the positions of the two singles forming the coincidence. Before coincidence sorting, the singles are checked for energy deposition; an energy window of 350 to 650 keV is typically used in order to accept all 511 keV photons and reject scattered photons that have lost a considerable amount of their original energy.

Ideally only *true* coincidences are detected by a PET scanner. By definition, a true coincidence is formed by the two annihilation photons originating from one radioactive decay event, and these photons have not underwent Compton scattering before detection. It is, however, not possible to say from a detected pair of photons whether they resulted from one annihilation event, or which is the true pair if more than two photons are detected within the coincidence window. Also a part of coincidences include one or two scattered photons. These types of events give rise to *random*, *multiple* and *scattered* coincidences, illustrated in Figure 2.4. In reality, for most of the singles detected by the scanner, a coincident photon is not found. This is because the other photon may be on such a trajectory that it does not intersect a detector element, or it may deposit insufficient amount of energy, or even pass the detector without any interactions. These single events cause random and multiple coincidences, and strain the processing electronics.

Random coincidences occur when two radioactive decays happen with a small time difference, and one photon from each decay event is detected. The length of the coincidence window affects the amount of random coincidences, but the time window cannot be boundlessly constricted because of limited temporal discrimination of events discussed in the next chapter (temporal resolution), and the time of flight difference of co-

incident photons. Random coincidences degrade the image quality and thus should be avoided or corrected for if possible. The rate of random coincidences C_R is given by:

$$C_R = 2R_T \cdot C_{SINGLE,1} \cdot C_{SINGLE,2} \tag{2.4}$$

where $C_{SINGLE,1}$ and $C_{SINGLE,2}$ are the rates of single events in a pair of detectors, and $2R_T$ is the coincidence window based on the temporal resolution R_T of the system. The rate of random coincidences increases with source activity. [10]

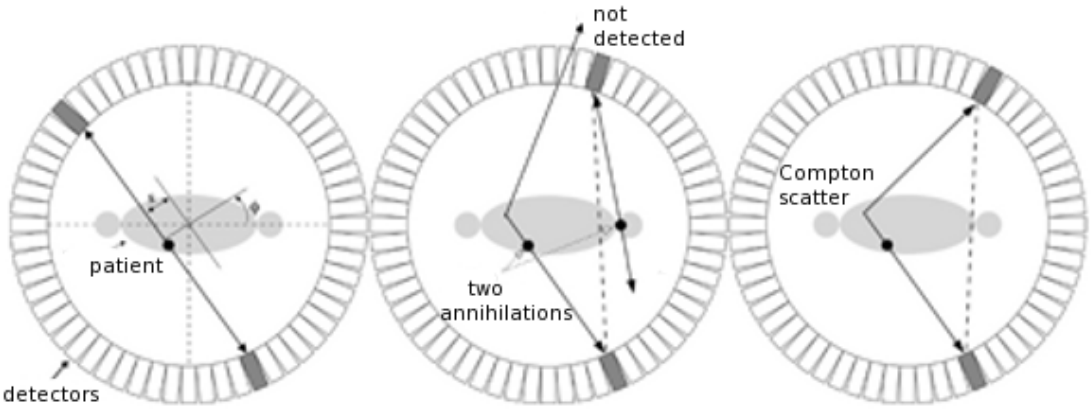

Figure 2.4: Transaxial view of a ring scanner. Left: A true coincidence. Middle: A random coincidence originates from two annihilation events happening at the same time. If more than two of the photons were detected, a multiple coincidence would be formed. Right: A scattered coincidence happens when one or both photons undergo Compton scattering. Adapted from [11].

Scattered coincidences originate from one radioactive decay, but one or both of the photons have scattered by Compton interaction in the FOV or within the scanner. As the direction of the scattered photon has changed, it is not possible to determine the correct LOR from the pair of photons, and the image quality is compromised. The amount of scattered coincidences can be reduced using a narrow energy window for singles, but this is limited by the energy resolution of the system and sensitivity requirements.

Multiple coincidences arise from the same issue as random coincidences, but in this case more than two singles are detected within the time window. Now the determination of the LOR becomes ambiguous. There are several possibilities in handling multiples, the easiest one is to simply discard all multiple coincidences. This may, however, lead to loss of considerable amount of data. Because most multiples include a true coincidence, it is often advantageous to try to recover the data. This could be done e.g. by forming coincidences of all pairs in the multiple that are in different modules of the scanner (in case of three singles in different modules, form three coincidences), or forming a coincidence of the pair of singles with highest energies (of three singles form one coincidence), or by some other rule. [12]

2.1.5 Performance characteristics

Obtaining good quality images that accurately reproduce the imaged object is a major concern in PET studies. The quality of images depends on the performance of the scanner, though it can be improved to some extent by corrective image reconstruction methods. The scanner's performance is associated with several, partly interdependent, parameters described below. To establish the performance criteria of PET scanners in practise, the National Electrical Manufacturers Association (NEMA) has developed guidelines on how the prime parameters should be evaluated. These guidelines are published as standards for clinical [13] and small animal PET [14]. They include standardized measurements for spatial resolution, sensitivity, scatter fraction, count losses and random coincidences as well as for image quality and accuracy of corrections. Some of these characteristics and related factors are discussed next.

Spatial resolution

The *spatial resolution* describes how small details can be seen in an image. It is defined by measuring the width of the profile obtained from an image of a very small object (a point-like source), expressed as the width of the profile at half of maximum value (full width at half maximum, FWHM). The resolution of a PET scanner depends on a number of factors. The first factor is the size of the scintillating elements in the detector, which gives the intrinsic resolution R_i as $R_i = d/\sqrt{12}$, where d is the width of the scintillator.

The second factor is β^+ emission characteristics: positron range and non-collinearity. An emitted positron travels a certain distance in tissue before being annihilated with an electron. The travelled distance, positron range, depends on the energy of the positron and thus the isotope that underwent the β^+ decay, and the medium. For example the effective positron range for F-18 in water is 2.2 mm. Since coincidence detection gives the site of annihilation instead of the site of the positron decay that holds the true spatial information, this error degrades the spatial resolution. The error (R_p) is determined from the FWHM of the positron count distribution, which for F-18 is 0.2 mm. Furthermore, as the two 511 keV photons are not emitted exactly at 180 degree angle, but with a deviation of even ±0.25°, the observed LOR does not intersect the position of the annihilation precisely. The error (R_a) produced by non-collinearity depends on the diameter of the scanner so that it approaches 2.0 mm in a large diameter full body scanner.

Additional errors to resolution can be caused by the chosen image reconstruction method (K_r), and the localization of an interaction in the detector when using block detectors instead of single detectors (R_l).

The overall spatial resolution (R_t) can thus be obtained by combining all the aforesaid factors:

$$R_t = K_r \times \sqrt{R_i^2 + R_p^2 + R_a^2 + R_l^2} \tag{2.5}$$

Which of the components of the equation are significant depends on the type and size of the scanner, and the used tracer. Experimentally the spatial resolution is measured from reconstructed images of point or line sources. As the spatial resolution of a scanner differs across the FOV, it is usually reported in the centre of the FOV and at a distance over in axial and transaxial directions. [9]

Sensitivity

The definition of the *sensitivity* of a PET scanner is the number of counts detected in a unit of time for the amount of activity in the source. Sensitivity is normally expressed as counts per second per megabecquerel (cps/MBq). It depends on several characteristics of the imaging system, such as the geometric efficiency, detection efficiency, energy window and the dead time.

The geometric efficiency is based on the detector's coverage of the solid angle projected by the source. This is affected by the size of the detector; decreasing the diameter and increasing the axial length both result in increased sensitivity, and vice versa. [9]

For a point source in the centre of a single ring detector, the sensitivity S based on geometric and detection efficiencies is described by the following equation:

$$S = \frac{A \cdot \varepsilon^2 \cdot e^{-\mu d} \cdot 3.7 * 10^4}{4\pi r^2} \tag{2.6}$$

where A is the area of detector seen by the source, ε is the detection efficiency, μ is the linear attenuation coefficient of the detector material for 511 keV photons, d is the thickness of the detector, and r is the detector ring's radius [15].

In practise the sensitivity of a detector is measured by scanning a source with known activity and counting the rate of coincidences in unit time C, and dividing the result with the source's activity A:

$$S = \frac{C}{A} \tag{2.7}$$

In a ring-shaped PET scanner the sensitivity is highest for the centre of the field of view and decreases towards the peripheries in axial and transaxial directions, due to the smaller solid angle covered by the detector, as seen by the source.

Noise equivalent count rate

Image noise depends on the number of counts per pixel, N, and is given by $noise = (1/\sqrt{N}) \times 100$. Noise can be reduced by increasing the amount of counts in the image, but in many cases this is not practical. In a PET image noise is characterised by *noise equivalent count rate* (*NECR*), that depends on true, scattered and random coincidence rates (C_T, C_S and C_R, respectively):

$$NECR = \frac{C_T^2}{C_T + C_S + C_R} \tag{2.8}$$

The signal-to-noise ratio of the final reconstructed image is dependent on noise equivalent count rate, thus NECR is a good performance characteristic of a PET scanner. [9] The noise equivalent count rate also depends on the activity of the source as with increasing activity, the count rates increase. At a certain level of activity, though, the rate of random and multiple coincidences begins to outweigh the rate of true coincidences, thus decreasing the NECR as function of activity.

Dead time

The count rate of the system is limited by another performance characteristic, *dead time*. The dead time is the time within the detector or the electronics of the system can not respond to another event because they are still processing the previous event. At high source activity the dead time can cause a significant amount of counts to be lost. [10] The system's dead time can be either *non-paralysable* so that the system does not recognise new events within a fixed time frame after a count, or *paralysable* so that all counts provoke the dead time which causes the system to paralyse at high event rates.

Temporal resolution

The *temporal* or *timing resolution* (R_T) describes the ability of a pair of detectors to determine the difference in time of arrival of two annihilation photons. It is typically in the range of 2 to 6 ns, and it affects the required length of the coincidence window so as not to reject coincident photons by accident. Thus the coincidence has to be 2 to 3 times the temporal resolution. [10]

Energy resolution

The *energy resolution* (R_E) of a PET scanner is defined as the FWHM of the 511 keV photon peak as seen in the energy spectrum of the collected counts. Energy resolution depends on the scintillation properties of the crystal and the efficiency of the photon detector. Essentially it means the detector's ability to determine the energy of the photon, which is important in order to reject scattered photons that have lower energy. [10] The energy resolution of the system restricts the length of the energy window applied to events; using too narrow a window might lead to rejecting 511 keV photons by accident.

Scatter fraction

Another characteristic is the *scatter fraction* (SF), given by:

$$SF = C_S / C \tag{2.9}$$

where C_S is the scattered count rate and C is the total count rate. [9] Scatter fraction describes the proportion of Compton scattered counts of all coincidence counts, which is important to know as these give an incorrect line of response and thus increase noise in image.

2.2 Axial PET technology

The current efforts in improving PET scanners are directed at improving the sensitivity and the spatial resolution of the devices. PET devices with enhanced performance would improve especially organ dedicated imaging, and imaging of small laboratory animals. Based on the attenuating property of the scintillating crystals, the sensitivity of a PET scanner can be improved by using longer crystals. This approach, however, quickly runs into a problem with reduced spatial resolution, as illustrated in Figure 2.5.

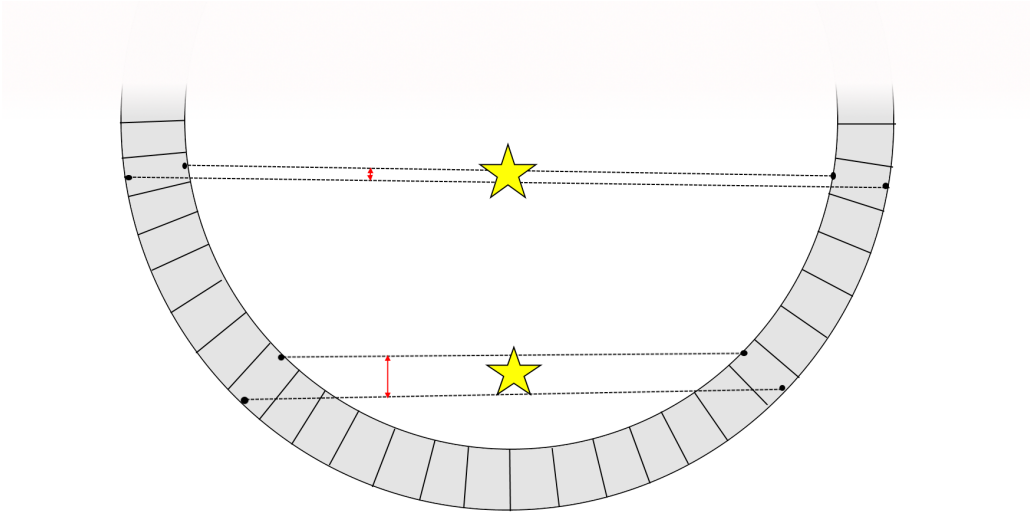

Figure 2.5: Parallax error (red arrows) is the uncertainty of the line of response, which increases towards the edges of the field of view in a conventional ring scanner where depth of interaction inside the crystals is unknown. The star symbols depict the site of annihilation.

Some of the photons that hit the detector surface in an oblique angle penetrate a crystal and are absorbed in an adjacent crystal. Without knowledge of the depth of interaction (DOI) in the crystal an error is added to the LOR of the coincidence. This parallax error is small close to the centre of the field of view, but increases towards the edges. Now if the DOI cannot be measured, increasing the length of the crystals is not feasible.

One approach to solve the problem of parallax error is gathering information on the DOI using layers of crystals, as in the HRRT scanner [4]. In this configuration, called the phoswich detector, the DOI information is collected by using crystals with two layers having different scintillation decay times. The total crystal length can thus be doubled without increasing the parallax.

Another approach, presented already in 1988 by Shimizu et al, used bundles of BGO crystals placed lengthwise in axial direction. The bundles of crystals were read on both ends with position sensitive PMTs. In this way it was possible to get the positions of singles in radial and tangential directions from the location of hit crystal in the bundle. The axial coordinate was obtained by calculation from the fractions of light collected at

both ends of the crystal. The axial resolution of this configuration (9.5 mm FWHM) was however not sufficient. [16]

The development of axial PET was later continued by the AX-PET collaboration. The first prototype used hybrid photon detectors to read bundles of YAP crystals at both ends, reaching axial resolution of 5 mm [17]. A new design of the system was made in 2007 that used wavelength shifting (WLS) strips that absorb and re-emit scintillation light, placed orthogonally to crystals to derive the axial coordinate. The crystals were now used to provide only the radial and tangential coordinates and the energy of the hits. [5]

In the new design of axial PET orthogonal layers of thin WLS strips are placed between layers of scintillation crystals in the matrix. Part of the scintillation light in the crystals is absorbed by nearby WLS strips and re-emitted on a shifted wavelength. This fluorescence light is read on one end of the strip by a photodiode. The scintillation light is able to escape the crystal only at angles larger than the angle of total reflection that depends on the refractive index of the crystal material. The operating principle is illustrated in Figure 2.6.

There are two main methods for deriving the axial coordinate from the light emitted by the WLS strips. Often more than one WLS strip responds to one single event in a crystal so that the consecutive responding strips form a cluster. In the most simple method the centre most strip of the cluster of responding WLS strips is considered and the z-coordinate of the single is set as the coordinate of the strip. Thus the spatial resolution in z-axis is discrete and determined by the width of the WLS strips. The second method takes into account the signals from all the strips that absorbed scintillation light from a hit. An analogue axial coordinate can be calculated from the signals using a centre of gravity algorithm. [5]

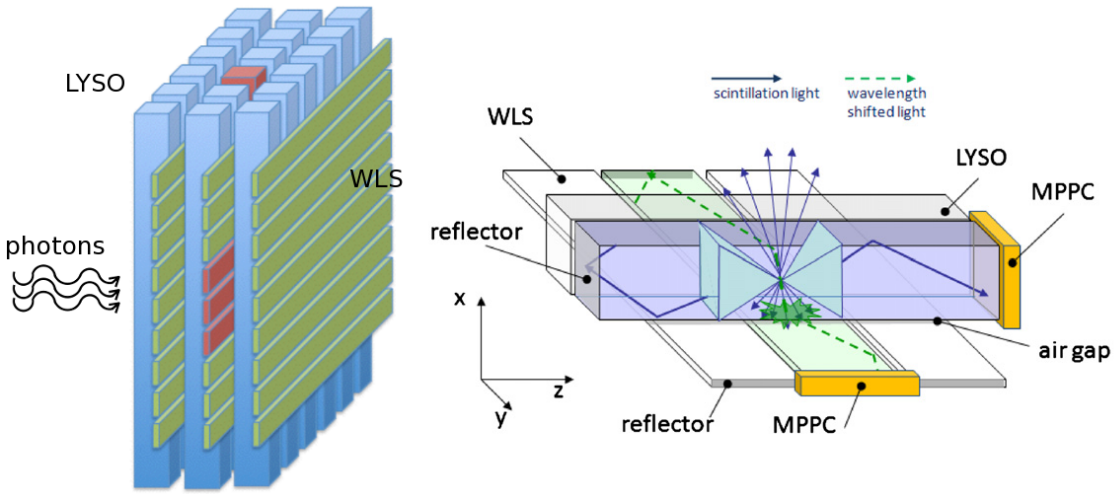

Figure 2.6: Left: Ax-PET module with a matrix of LYSO crystals and WLS strips behind the rows of crystals. Right: Part of scintillation light escapes the crystal and is absorbed and re-emitted by the WLS strip. [18]

An AX-PET demonstrator with two modules having 48 LYSO crystals and 156 WLS strips, all read out by geiger-mode avalanche photodiodes, was built by Beltrame and colleagues, as reported in 2011 [19]. The results were promising; spatial resolution of under 2 mm FWHM was achieved in all three dimensions for a tomographic reconstruction of a point source. The resolution remained homogeneous over the whole field of view [20].

Another prospect of axial PET is corrections for inter-crystal scattering (ICS) events. Inter-crystal scattering arises from Compton scattering of a photon inside the detector so that it transfers energy to more than one crystal. Currently ICS events are handled only with a high low-energy threshold which excludes part of these events, but at a cost of sensitivity. Recording the ICS events is possible with the AX-PET system, so correction methods were studied by Gillam et al. The fraction of ISC events being about 20 %, the results show 5 to 10 % increase in image quality without loss of spatial resolution when inclusion method was used. [21]

3 MONTE CARLO SIMULATIONS

Monte Carlo methods are used to solve problems that have inherent random properties and are thus difficult to solve analytically. Simulations using Monte Carlo methods are important in nuclear imaging due to many stochastic processes involved. In addition, simulations provide a tool to examine the various factors that contribute to the data such as noise, biological variability, scattered radiation or the detection system. In order to simulate a system with a stochastic process four things are needed to know: a) the processes that can happen, b) the probability of occurrence, c) a random number, and d) the environment.

For simulating random events random numbers are needed. There are tables of random numbers collected from real random events like radioactive decay, but tables lack the required length to run large simulations, so computer-generated random numbers are required. It is not possible to generate truly random numbers, but instead deterministic algorithms are used to produce *pseudo random* numbers, that have many of the characteristics of randomness. A simple (pseudo) random number generator (RNG) is the linear congruential generator that gives the next sample from the *n*th sample I_n:

$$I_{n+1} = (aI_n + c) \bmod m, \tag{3.1}$$

where a, c and m are the chosen parameters, and I_0 is the *seed* or the *start value*. The problem with the linear congruential generator is that it starts repeating itself quickly and is thus not appropriate for most applications. [22] There are still many good RNGs available, such as the Mersenne Twister [23]. Most RNGs sample a uniform range of integers that can be transformed into a range such as [0,1], **U**[0,1], by division. Often distributions other than uniform are needed, so sampling of the distribution is needed. Two main methods to create desired distributions are the *inversion method* and the *acceptance-rejection method*.

Both methods make use of probability density functions (PDF) that give the probabilities of outcomes for a random sample from the distribution to transform uniform distributions into other distributions. The PDF of **U**[0,1] is

$$p(x) = \begin{cases} 1, when\, 0 \leqslant x \leqslant 1 \\ 0, otherwise \end{cases} \tag{3.2}$$

Also the cumulative distribution function (CDF) which is the integral of PDF is often used in sampling. In the inversion method to get values from a distribution, for example exponential distribution, the following steps are taken: 1) Pick a sample u from **U**[0,1], 2) Find u on the y-axis of the CDF of the target function, 3) Find value x that corres-

ponds to *u,* so that *F(x) = u*. The inversion method can be used only if the target CDF is invertible. In case it is not invertible or the inversion is computationally heavy, the acceptance-rejection methods can be used. In this method, sampling from a difficult PDF is replaced with sampling from an easy PDF. To use the acceptance-rejection method for *f(x)*: 1) Choose an easy-to-sample PDF *g(x)* and a constant *c* so that

$$c * g(x) \geq f(x), \tag{3.3}$$

2) Generate a random number *v* from *g(x)*, 3) Generate a random number *u* from **U**[0,1], 4) If the generated numbers satisfy

$$c * u < \frac{f(v)}{g(v)}, \tag{3.4}$$

then accept the random sample from the desired distribution *v,* otherwise reject *v* and continue from step 2. [22] In case using either of these two methods alone is problematic when developing an algorithm, a mixture of both can be used [24].

3.1 Simulations in medical imaging

Medical tomographic imaging can be dived into two types: transmission (e.g. x-ray CT) and emission (PET, SPECT) tomography. Both types are based on detecting photons, so the simulation must include the source of photons, the interactions of photons with matter, and the conversion of the interactions into detected events. A model of the physical processes at each step is needed for simulation. The process models can be either deterministic (in analytical simulations) or stochastic (in Monte Carlo simulations), in practise most simulations include both deterministic and stochastic elements. [22]

When using Monte Carlo simulations accuracy is dependent on the probability functions, i.e. the cross-sections, of interactions. The cross-section, a hypothetical area, is the probability at which a particle will interact with another particle, and can be defined for a specific process or total attenuation. For example a photon with 1 MeV energy has a cross-section of $1.17*10^{-9}$ cm^2/g for photoelectric absorption in hydrogen, as calculated with the XCOM online database [25]. The cross-section tables are used in modelling attenuation of photons in matter, as well as the other physical processes. The most important processes when simulating nuclear imaging are photoelectric effect, Compton scattering, Rayleigh scattering, positron annihilation and radioactive decay. Considering the travel of a photon in a medium we need to know its position, direction and energy to calculate the path length, i.e. the distance it travels before interacting with the medium. The mean path length follows an exponential distribution (Equation 2.3), and is calculated using the cross-section data that is sampled to find the location of interaction. The cross-sections thus gives the specific attenuation coefficients for materials. As the location of interaction is known, the type (absorption, scattering etc.) is determined again using sampling of the cross-section data. [24]

3.2 Geant4

Geant4 is a simulation toolkit for tracking particles that pass through matter, by applying Monte Carlo methods. The main domains of simulations include geometry and materials, particle interaction in matter, tracking, hit and event management, visualization and user interface. Geant4 contains a large number of physics models for photons, electrons, muons, hadrons and ions, of which the user can choose, and the set of physics processes is large in order to serve the needs of a variety of fields of research. The used data about particle interactions has been drawn from many accredited sources, and a number of random number generators are available. [26]

To make Geant4 a flexible tool and allow for further development, it was written in C++ using object-oriented technology. The modular structure allows compiling and using only the necessary components, and extending functionality as required by the user. Geant4 source-code is available at the collaboration's site [27].

3.3 GATE

GATE, short for Geant4 Application for Tomographic Emission, is designed and developed by the OpenGATE collaboration [28]. It is a simulation toolkit specifically designed for nuclear medicine, including optimizations and tools for PET and SPECT imaging studies. Knowledge of C++ programming is not needed to use GATE as the simulations are written in scripting language.

The architecture of GATE is based on Geant4, making use of its extensive physics libraries. On the developer layer of GATE basic tools such as geometry definition, time management, source definition, detector electronics modelling and data output are defined. The user layer allows running simulations both batch-wise using scripts and interactively.

For defining the geometry of the modelled scanner, GATE has specific, predefined geometric hierarchies called systems. The systems are needed to correctly process the Geant4 particle interaction histories, *hits*, into realistic detector output. For PET GATE provides a system to create a ring scanner that allows integrated coincidence sorting and data output as list mode and sinograms.

One major addition that GATE brings into the features of Geant4 is the management of time-dependent phenomena. This allows simulation of realistic scanner rotation, patient movement, changes in activity distribution, *et cetera*. Because Geant4 requires the geometry to be static during a simulation, simulations with movement are divided into smaller time steps, and the geometry is updated at the beginning of each time step.

Several types of sources can be modelled with GATE, e.g. radionuclides, gamma-rays, positrons, etc. Besides the type, user can define the source's volume and position, direction of emission, energy spectrum and activity. The half-lives of radionuclides are drawn from the Geant4 database. Voxelized data from phantoms or patients can also be

used as sources, since GATE can convert emission data into activity levels, and grey scale image into material definitions.

The electromagnetic physics used in GATE are derived from Geant4. The physics package manages positrons and electrons, gamma-, x- and optical photons, muons, hadron and nuclei. Two different packages can be used: standard energy (100 keV and above) and low energy (250 eV and above) that includes also Rayleigh scattering. Specific thresholds, cuts, can be applied to the production of secondary particles like electrons, x-rays and delta-rays to increase simulation speed. [29]

The properties of materials are defined in a materials database that can easily be modified by the user. The material database consists of elements and materials which are combinations of elements. Of elements GATE stores the name, symbol, atomic number and molar mass. For materials the name, density, constituent element(s) and their abundances are stored. [12]

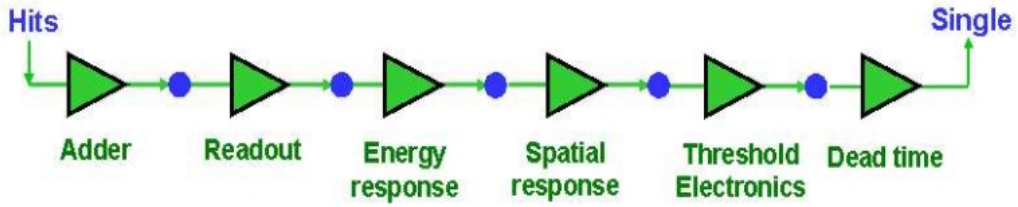

Figure 3.1: The digitizing in GATE processes hits, particle interaction events, into a single, the detected signal. Each digitizer module processes the input independently. The intermediate output of a module is called a pulse. [12]

To simulate the electronics response of a detector, GATE has the digitization process. Digitization converts particle interactions (which are referred as hits) into detected singles and coincidences. In order to record the hits in the detector and the FOV, two types of sensitive detectors are defined: the *crystal* and, optionally, the *phantom*. The interactions are then processed into singles and coincidences inside the digitizer chain. The digitizer chain consists of a number of processing modules. An important digitizer module is the *adder* which sums the energy deposited into a crystal by a particle during consecutive scattering and photoelectric events, i.e. a series of hits in one crystal, into a pulse. The position of the pulse is computed to be the energy-weighted centroid of the hits. For a particle that scatters through several crystal elements a list of pulses is generated. [12] GATE has also other digitizer modules called user modules that can be used to modify the pulses into realistic detector output signals. With the user modules several characteristics of the scanner such as level of readout, energy resolution, temporal resolution, energy thresholding, dead time, and finally coincidence sorting, can be modelled. The digitizing process is presented in Figure 3.1. It has been shown that the electronic processing of PET can be accurately modelled using GATE. [30] It is also possible for the user to make new digitizer modules by expanding a general frame of a module with new functionality.

For coincidence sorting GATE offers two methods. In the first method a detected single opens the coincidence window to search for a second single within the window. For this duration no other single can open its own coincidence window. In the second method all singles open a coincidence window and coincidences are searched using a logical OR operation between all the signals. Multiple coincidences can be handled per user's choosing with nine different multiples policies, the most common of which is discarding all multiples, the *killAll* policy. [12]

4 MODEL CONSTRUCTION

The AvanTomography project is based on the same concept as the AX-PET [5]. The construction of an earlier version of AvanTomography is described in the MSc thesis of T. Zedda [31]. In the latest version the systems was upgraded to have a set-up of 6 modules, each module having 5 scintillating crystals and rows of WLS strips to read the two layers of crystals.

In this chapter the construction of the model used in Monte Carlo simulations is described, firstly the geometry and material definitions and secondly the model for axial coordinate determination and its implementation. The work was done using the GATE simulation toolkit described in Chapter 3.3.

4.1 Module geometry and materials

For this thesis work, a ring shaped scanner geometry was created with GATE to model the demonstrator. The scanner was divided into sectors in which the modules were placed. The modules could then be copied inside the sectors to create a layered structure, or moved and rotated to create different configurations. The crystals and the WLS strips were modelled as physical components, but the photon detectors used to read out both crystals and WLS strips (Multi-pixel photon counter, MPPC by Hamamatsu [32]) together with the processing electronics were modelled using a GATE digitizer chain that simulates the signal processing. A schematic of a module is presented in Figure 4.1.

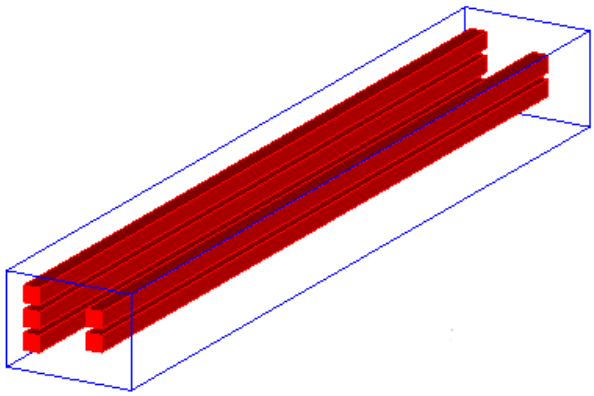

Figure 4.1: A schematic view of a module with five LYSO crystals in two layers. Rows of WLS strips (not shown here) are placed orthogonally to the two layers of crystals.

Scintillating crystals

The scintillating crystals chosen for AvanTomography project are PreLude®420 LYSO crystals produced by Saint-Cobain [33]. The chemical form of LYSO is $Lu_{1.8}Y_{0.2}SiO_5$. Properties of PreLude420 crystals are shown in Table 4.1. The crystals used in the project have a cross section of 3×3 mm^2 and are 150 mm long.

Table 4.1: Properties of PreLude420 LYSO crystal [33].

Density	7.1 g/cm^3
Attenuation length for 511keV	1.2 cm
Energy resolution	8.0 %
Wavelength of emission max	420 nm
Refractive index	1.81
Decay time	41 ns
Light yield	32 photons/keV

LYSO material was added into GATE material database using mass fractions of elements as presented in Table 4.2.

Table 4.2: The mass fractions of elements composing LYSO crystals in GATE material definition.

Element	**Mass fraction**
Lutetium	0.7145
Yttrium	0.0403
Silicon	0.0637
Oxygen	0.1815

Most of the lutetium in the PreLude420 crystal is stable ^{175}Lu, but it also contains 2.5 % of a radioactive isotope ^{176}Lu which is a naturally occurring β^- emitter with a half-life of $3.8*10^{10}$ years. ^{176}Lu decays to ^{176}Hf 196 keV excited state 0.34 % of the time, and to 597 keV excited state 99.66 % of the time. The 597 keV state of ^{176}Hf releases excitation with a cascade of three gamma rays of 307, 202 and 88 keV. The PreLude crystal absorbs close to 100 % of the beta particles, but some of the de-excitation photons escape the crystal. The intrinsic activity of LYSO is 39 cps/g which means the activity of one crystal with a volume of 3×3×150 mm^3 and density of 7.1 g/cm^3 is about 374 Bq.

Wavelength shifting strips

The wavelength shifting strips used in the demonstrator are EJ-260 plastic scintillators by Eljen Technology. EJ-260 absorbs light and re-emits it on the visible green light region, the peak emission being at 490 nm. EJ-260 is made of polyvinyltoluene and has

density of 1.023 g/cm^3. [34] The WLS strip material was added into GATE with mass fractions of 0.5263 for hydrogen and 0.4737 for carbon.

Module

The dimensions of each demonstrator module are 24×17×154 mm^3 so that the 17×154 mm^2 side of the module is facing the FOV while 154 mm is the axial length. The modules are plastic with 2.7 mm thick walls, and another wall inside the module separating the rows of crystals. The crystals are arranged inside a module in two layers; the first layer having three crystals and the second two. The crystal pitch on each layer is 4.2 mm and the spacing between the two layers is 5.6 mm. A row of WLS strips is placed around each layer of crystals so that most of the length of the crystals are covered, leaving just smalls gap at the very ends. A geometry model corresponding to the physical module and the crystals and WLS strips within was constructed as part of this thesis.

4.2 Analytical model for axial coordinate reconstruction

In the AvanTomography demonstrator, when a photon interacts with a crystal, a number of scintillation photons are generated inside the crystal. Some of these optical photons escape the crystal and hit the WLS strips. The WLS strips absorb the optical photons and re-emit them at a shifted wavelength, and a part of the photons are detected by the MPPC attached to the strip. With GATE it is possible to simulate the scintillation processes and optical photon transport by activating the necessary physical processes and defining the optical properties of all the materials and surfaces. Using optical processes will, however, increase the simulation time dramatically since for example a 511 keV hit to a LYSO crystal will produce roughly 16,000 scintillation photons that then need to be individually tracked. In addition it is not a trivial task to determine all the optical properties of the materials and surfaces needed in the simulations. It was therefore decided to implement an analytical model for axial coordinate determination with WLS strips. The used model, described below in more detail, is based on the work of P. Solevi and colleagues in the AX-PET project [35].

4.2.1 The analytical photon transport model

In the AX-PET project model, the distribution of photons in the WLS strips depends on the energy E_n deposited into the LYSO crystal, the axial distance between positions of the interaction z_n and the strip z_i, and the depth of interaction x_n within the crystal. It is assumed that the response does not depend on which side of the crystal the WLS strips are, so only the axial position of a strip (z_i) is taken into account. The equation (4.1) gives the number of photoelectrons in a WLS strip, so that when resolved for a row of

strips, the photoelectrons form a Gaussian distribution that peaks in the strip closest to the interaction n. A series of hits ($n>1$) can results in several peaks forming.

$$N_{pe(i)}=\sum_{n=1}^{N} A(x_n, E_n)\cdot \mathrm{e}^{-\frac{(z_n-z_i)^2}{2\sigma_{xn}^2}} \tag{4.1}$$

In the equation index *i* is the label of the WLS strip and the sum is consequently calculated for all strips reading the crystal. Index *n* labels the photon's interaction in the crystal as it may scatter and deposit energy more than once. [35] Figure 4.2 shows a schematic view of the variables in the equation. The signal amplitude *A* depends on the depth of interaction x_n and the deposited energy E_n. However as the variation in x_n is small, less than 3 mm, and the signal *A* is linearly dependent on the energy so that $A(En)=A(511\,keV)\cdot En/511\,keV$, the equation can be reduced into the following form:

$$N_{pe(i)}=\sum_{n=1}^{N} A(511\,keV)\cdot\frac{E_n}{511\,keV}\cdot \mathrm{e}^{-\frac{(z_n-z_i)^2}{2\sigma^2}} \tag{4.2}$$

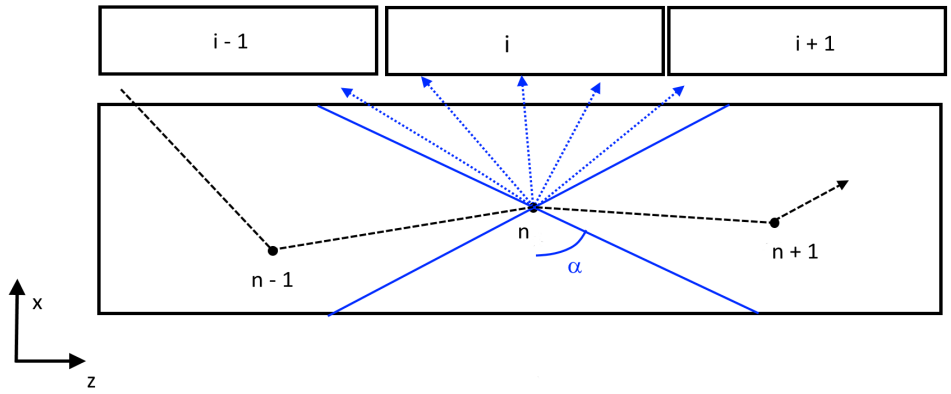

Figure 4.2: A schematic 2D view of a LYSO crystal and WLS strips. The black dashed line represents the 511 keV photon that is attenuated inside the crystal. A hit (n) creates scintillation photons (blue dotted lines) that escape the crystal only within the angle of total reflection (blue solid lines).

4.2.2 Parameter determination

For this thesis work, the parameters *A(511 keV)* and *σ* were determined according to the properties of the components used in AvanTomography demonstrator. As no measurement data was available, the parameters are determined based on purely theoretical consideration of the yield and transport of optical photons. The result of the Equation 4.2 is

thus the number of optical photons in strip i instead of the number of photoelectrons, which would be the realistic measure. Thus, parameter σ was calculated from the length of the crystal surface from where the photons can escape the crystal. From Snell's law we get the angle of total internal reflection at the crystal–air surface to be:

$$\theta_1 = \arcsin\left(\frac{n_2}{n_1} \cdot sin\theta_2\right) = \arcsin\left(\frac{n_2}{n_1}\right) = 33.5\,^\circ, \tag{4.3}$$

Where θ_1 is the angle of total reflection, θ_2 is 90 degrees (the critical angle of the refracted ray), n_2 is the refractive index of air and n_1 is the refractive index of LYSO (see Table 4.1).

Now let us consider a hit in the middle of a crystal in x- and y-axis. As width of the crystal is 3 mm and the angle θ_1 is 33.5°, using trigonometry the length l_z on the crystal surface on the side of the WLS strips from which the photons can escape is 4.57 mm.

The scintillation photons created by a hit disperse as a sphere with even distribution, thus the distribution of photons seen on a flat surface like the crystal edge is Gaussian. Because there is a gap between the crystal and the WLS strips over which the photons disperse further, we can approximate that the length l_z is the full width at tenth maximum (FWTM) of the distribution on flat surface. From the definition of FWTM it is possible to get the parameter σ:

$$FWTM = 2\sqrt{2\ln 10}\,\sigma \Leftrightarrow \sigma \approx 1.07 \tag{4.4}$$

From the Gaussian distribution of photons, it is also possible to calculate the signal peak *A(511keV)*. A light yield of 32 photons/keV (Table 4.1) gives the number of generated photons to be about 16,000 for 511 keV. Assuming that the scintillation photons' initial track is evenly distributed in full solid angle, we get the percent of photons that exit the crystal face towards the WLS strips to be 20.5 %, which is about 3,400 photons. The integral of a general Gaussian curve can be reduced to:

$$\int_{-\infty}^{\infty} Ae^{-((x+b)^2/2\sigma^2)}\,dx = A|\sigma|\sqrt{2\pi} \tag{4.5}$$

As we know the result of the integral to be 3,400, we can get signal peak:

$$A(511\text{kev}) = \frac{3400}{c\sqrt{2\pi}} \approx 1270 \tag{4.6}$$

Finally, Equation 4.2 with parameters *A(511keV)*=1270 and σ=1.07 is implemented into GATE source code to calculate the distribution of optical photons that reach the WLS strips. The equation does not give the actual number of photons that reach the strips since it does not account for e.g. attenuation of the scintillation photons, nor the amount that reaches the MPPC at the end of a strip. It does, however, model the pattern of firing in the rows of WLS strips. The photoelectric yield of WLS strip could be roughly estimated with the equation presented in the article by Braem et al., in case parameters like the efficiencies of the strips and the MPPCs are known [5]. Equation 4.2 with the obtained parameters is implemented into GATE source code as part of the signal processing chain that emulates the processing in the photon detectors and the electronics.

4.2.3 Axial coordinate determination

As the amount of photons in WLS strips can be calculated using Equation 4.2, the responses of WLS strips of the row can be used to determine the axial coordinate of the single. The axial coordinate can be determined in a continuous scale based on the amount of photons detected in each strip, but in this project a simpler, discrete method was used. This method and the solution for the data output of the real demonstrator are described in the MSc. thesis of S. Moradi [36]. In the discrete method, each WLS strip in which any amount of photons is detected is considered “fired”, having value 1. All other strips are considered not fired, i.e. 0. As the scintillation photons spread inside the crystal, it is likely that more than one strip close to the event location is fired, and therefore fired adjacent strips form a cluster.

Depending on whether the size of the cluster is odd or even, the axial coordinate is considered the position of the centre most strip or the midpoint between the two centre most strips in a cluster, respectively. Scattering of the annihilation photon along the length of the crystal can result in more than one cluster in the row of WLS strips, in which case the biggest cluster is chosen for coordinate determination.

There are also some cases in which the axial coordinate can not be determined reliably and the single is therefore discarded. The first and the second case are that no strips are fired by the single, or the size of the cluster is 1. One of these might happen if the energy deposited by the single is very low, or the single occurred in either end of the crystal that are not covered by WLS strips. In the third case there are more than one cluster of the same size, but as we cannot say which one is the best choice, determining the axial coordinate is not possible and the single is therefore discarded.

4.3 The new digitizer module

The digitizer module *adder* is used in GATE to merge hits that result from a particle's scatter and absorption events in one crystal to form a pulse. Consequently the exact positions of the individual events are lost. This corresponds to the readout of a crystal with a photon detector at the end of the crystal in radial scanner geometry. However in AvanTomography demonstrator the crystals are arranged axially and the z-coordinates of pulses are read using WLS strips, and the axial coordinates of the pulses would be lost if the pulse locations were merged. For this reason the existing pulse adder module could not be used, but instead a new digitizer module was developed as part of this thesis work. The new digitizer module, GateWLSProcessor, sums the energies of a photon's interactions inside one crystal, and determines the z-coordinate by simulating the response of WLS strips. Figure 4.3 shows the added classes and their relation to the existing digitization in GATE.

4.3.1 The pulse processor class

Digitizer modules (also referred to as pulse processors) are added into GATE source code by expanding the base-class GateVPulseProcessor. The role of the modules is to receive a list of pulses (consisting of events of one annihilation photon) from the Digitizer, process the pulses, and return a new list of processed pulses, which can then be fed to another processing module or to coincidence sorting. GateVPulseProcessor defines two functions for the processing. The first one is ProcessPulseList that receives the list of unprocessed pulses, calls the other function, ProcessOnePulse for each pulse in the list, and finally returns the list of processed pulses. ProcessOnePulse is a function that processes one pulse (for example, adds Gaussian blurring to the energy of the pulse to simulate the energy resolution of the scanner) and incorporates it into the list of processed pulses.

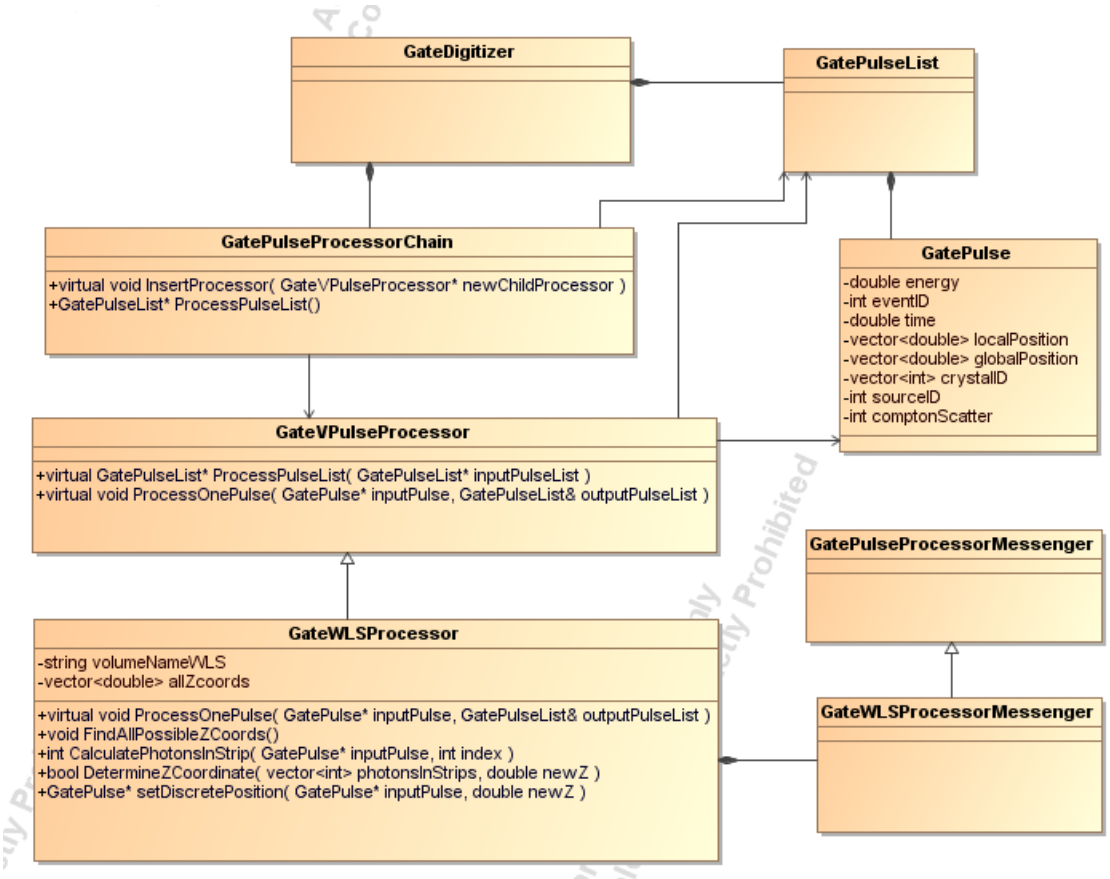

Figure 4.3: The GateDigitizer has chains of Pulse Processors that process the pulses stored in lists in the Digitizer. The new GateWLSProcessor is used to determine the z-coordinate of each pulse when simulating axial PET. The messengers are used to handle the input and output of the pulse processors.

For the pulse processing of an axial geometry scanner, class GateWLSProcessor was created from the base-class GateVPulseProcessor. The existing functionality of the function ProcessPulseList was considered suitable for the new pulse processor, so the

task was to write the functionality of WLS signal processing into ProcessOnePulse. The helper functions defined in the GateWLSProcessor class (see Figure 4.3) are called by the function ProcessOnePulse.

Digitizer modules are taken into use by inserting the module into the digitizer with a script command. To create the necessary script commands each module has its own messenger class. For GateWLSProcessor a messenger class GateWLSProcessorMessenger was created so that the module could be taken into use and parameters could be conveyed to the processor. The current implementation requires only one parameter, the name of the physical WLS geometry as defined in the geometry script, to be given to the processor.

4.3.2 Processing of one pulse

Processing of a pulse is done in function ProcessOnePulse that has three main functions: handling intra-crystal scattering, setting z-coordinate of a pulse according to WLS strip firing, and discretising the x- and y-coordinates of the pulse. The input parameters of ProcessOnePulse are inputPulse, i.e. the pulse to be processed, and outputPulseList, i.e. the list of already processed pulses. A pulse contains information on the energy, local and global position, timing and scattering of the pulse, the identification of the crystal in which the pulse is produced, and identification of the source and annihilation event that originated the pulse. A flow chart of ProcessOnePulse is shown in Figure 4.4. For clarity, the functionality is divided into five steps that are explained next with more detail.

In here the coordinate space (Cartesian x, y and z) refers to the local space within a module where the z-axis is along the crystals. To make a scanner, the modules can be individually translated and rotated so that the local module coordinate space differs from the global coordinate space. The pulse locations are handled in local spaces and then transformed into the global space.

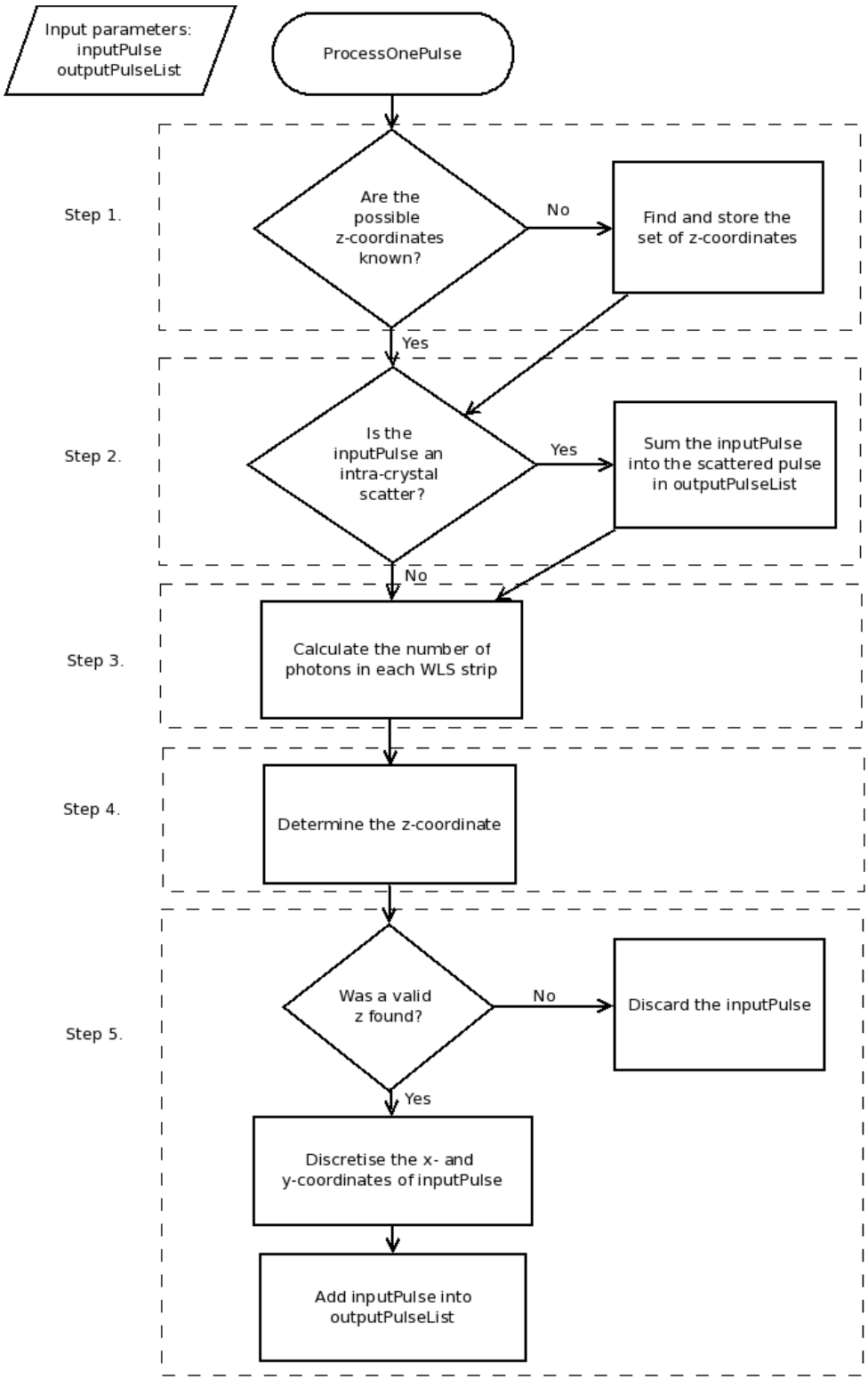

Figure 4.4: A flow diagram of function ProcessOnePulse. The function takes inputPulse and outputPulseList as parameters, processes the inputPulse, and adds the processed inputPulse into outputPulseList. The functionality is divided into five steps that are explained in detail in this chapter.

Finding the discrete z-coordinates

Function FindAllPossibleZCoords was created to find the set of discrete z-coordinates that can be set as pulse location. The function searches for the physical repeated geometry of the row of WLS strips using the script name of the geometrical object, to find out the number of WLS strips in a row, *numWLS*, and the centre-to-centre distance between two consecutive strips, *pitch*. From these two values it calculates the centre coordinate of the first WLS strip, firstZ. Using this basic information the function calculates the z-coordinates as the centre points of all the strips and the centre points of the gaps between consecutive strips. In the local space of a module the coordinates are set in symmetry around z=0 plane, and they are stored for later use into vector *allZCoords*. The algorithm is described below:

```
FindAllPossibleZCoords
 1  numZCoords ← 2 * numWLS - 1
 2  halfPitch ← pitch / 2
 3  firstZ ← - numWLS / 2 * pitch + halfPitch
 4  currentZ ← firstZ
 5  for 0 < i < numZCoords
 6     allZCoords[i] ← currentZ
 7     increment currentZ by halfPitch
 8     increment i by 1
 9  end for
```

Merging intra-crystal scattered pulses

All the pulses in the inputPulseList in function ProcessPulseList are the result of a single particle (photon) scattering and being absorbed inside the detecting elements of the scanner. When an inputPulse is processed in ProcessOnePulse, it is checked if one of the pulses in the outputPulseList is located in the same crystal as the inputPulse. Because it is not possible to register these separate events within one crystal with a real detector, the pulses are merged. In the merge process the deposited energy of the pulses are summed and the coordinates of the pulse locations are merged. Merging is done using the already existing CentroidMerge function of the Pulse class that determines the location of the merged pulse with an energy-weighted average of the two originals. Using merge results in loosing the individual z-coordinates of the pulses which is not desired in axial PET, so before the merge, the responses of the WLS strips are calculated and stored into vector *photonsInStrips*. This method generates two clusters to the vector of photons if the scattering length within the crystal is long (more than 4.6 mm in z-direction), though usually the scattering length is much shorter and merging affects only the signal amplitude of the cluster.

```
1  determine WLS strip response for inputPulse and store it into photonsInStrips
2  for each pulse in the outputPulseList do
3     if crystalID of currentPulse in outputPulseList = crystalID of inputPulse
4        determine WLS response for currentPulse and add it to photonsInStrips
5        merge inputPulse into currentPulse
6  end
```

Calculating photons in strips

Equation 4.2 with parameters *A(511keV)*=1270 and σ=1.07 (see Chapter 4.2.2) is implemented in GateWLSProcessor class in member function CalculatePhotonsInStrip. The function is repeatedly called for each WLS strip in a row, while the output is stored in vector *photonsInStrips.* The function takes the pulse (inpuPulse or the currentPulse of outputPulseList) and the index *i* of current WLS strip of the vector as input, and returns the amount of photons created by the pulse to the current WLS strip. The only parameter that varies between the calls is the index of the strip that is needed for calculating the distance from the location of the pulse to the strip in z-axis, the $(z_n - z_i)$ of Equation 4.2.

```
CalculatePhotonsInStrip(Pulse, i)
1  energy ← energy of Pulse
2  zStrip ← allZCoords[2 * i]
3  zPulse ← z coordinate of Pulse
4  numPhotons ← A511 * (energy/E511) * exp( -((zPulse – zStrip)^2 / 2σ^2))
5  return numPhotons
```

Determining the z-coordinate

Determination of the z-coordinate of the pulse is done in member function DetermineZ-Coordinate that takes as input a vector of photons (*photonsInStrips*) and returns the discrete z-coordinate. The theoretical method of searching the z-coordinate was presented in Chapter 4.2.3. The algorithm in function DetermineZCoordinate is described below. Due to higher level organisation of pulse processing, a maximum of two clusters are found in the vector *photonsInStrips.* The algorithm searches for the indices of the starting points of the clusters and stores them together with the sizes of the clusters (i.e. the number of non-zero strips found in succession). The z-coordinate is chosen from the vector *allZCoords* constructed previously, using the size and location of the biggest cluster found. In case the z-coordinate cannot be determined due to invalid cluster size, an error message is sent back to the caller function ProcessOnePulse, where the pulse is discarded.

```
DetermineZCoordinate(photonsInStrips)
 1  for 0 < i < numWLS
 2     if photonsInStrips[i] > 0
 3        if photonsInStrips[i - 1] = 0
 4           index ← i
 5        else
 6           size ← size + 1
 7  end for
 8  if no cluster was found, or the clusters are the same size, or the size of the only
    cluster = 1
 9     return error
10  centre ← index + size / 2 – 0.5
11  newZ ← allZCoords[2 * centre]
12  return newZ
```

Discretising the pulse location

GATE allows tracking particles with high precision and consequently shows the exact intra-crystal locations for all pulses. Getting such high resolution information is, however, not possible with real PET scanners, but the precision of location of singles is dependent on the size of the crystals. The location of the singles is usually defined to be the centre of the crystal in all axes. GATE has a dedicated digitizer module for this task, but using it for axial PET would result in loosing the axial coordinate. Thus, a discretisation for just the x- and y-coordinates was added into ProcessOnePulse of WLSProcessor. In this process the x- and y-coordinates of the pulse are set to be at the centre of the crystal, i.e. x=0 and y=0 in the intra-crystal space. The z-coordinate that is obtained from DetermineZCoordinate is already discrete so no further processing for this third coordinate is needed. The crystal class includes a function for transforming coordinates into any higher-level space that was used to get the global coordinates corresponding to the new discrete local coordinates. The new coordinates are stored into the pulse as variables *localPosition* and *globalPosition*.

```
SetDiscretePosition(Pulse, newZ)
1  newLocalPos ← (0, 0, newZ)
2  localPosition  ← newLocalPos
3  transform newLocalPos into global space as newGlobalPos
4  globalPosition ← newGlobalPos
```

5 SIMULATION SETS

The simulations were run on GATE version 7.0 that uses version 9.6.3 of Geant4. The installation of GATE was validated by running a PET benchmark simulation and comparing the results against given validation data. The details of the simulations are described in this chapter. Module geometry is the default one described in Chapter 4.1, while the scanner geometry is described with each simulation set up.

A low energy electromagnetic physics package was chosen to set up required processes. The package includes the following physics processes: photoelectric effect, Compton scattering, Rayleigh scattering and gamma conversion for photons, multiple scattering, ionization, bremsstrahlung and annihilation for electrons and positrons, and atom de-excitation. These are implemented using the Penelope models that have been developed specifically for Monte Carlo simulations in energy range of about 200 eV to 1 GeV [37]. The Mersenne Twister RNG was chosen for generating random numbers, and automatically switching seed was used.

The digitizer modules included in the simulations with used parameters are listed in Table 5.1 and Table 5.2. For the singles processing, external energy blurring was added to account for the crystals intrinsic and the electronics' energy resolution at the level of the annihilation photon energy. An energy window was set to limit the amount of scattered and intrinsic coincidences. Dead time of the system is set to be the integration time, 3 μs, over which all hits in one crystal are piled up into one single event, with a non-paralysable scheme. Dead time is only applied to singles processing since the processing of coincidences is done offline and thus has no processing inefficiency. A temporal resolution of 0.25 ns was used to account for the time discrimination capability of the MPPCs.

Table 5.1: Digitizer modules with parameter values for processing Singles

Module name	Parameter	Value
WLS Processor	Volume name	“wls”
Blurring	Energy resolution	0.127
	Energy of reference	511 keV
Thresholding	Threshold	350 keV
Upholding	Uphold	650 keV
Dead time	Dead time	3000 ns
	Mode	non-paralysable
	Volume name	“crystal”
Temporal resolution	Time	0.25 ns

Table 5.2: Digitizer modules with parameter values for processing Coincidences

Module name	Parameter	Value
Coincidence sorting	Window	10 ns
	Multiples policy	killAll
	Minimum sector difference	1
	All pulses open coincidence gate	true

For the coincidence processing, a window of 10 ns was used. All multiple coincidences were discarded, and as the demonstrator has only four sectors, coincidences forming between neighbouring modules were accepted. The chosen coincidence gating corresponds to offline coincidence processing that causes no count losses at high count rates.

5.1 Validation of the model

In order to validate the Monte Carlo model of the AvanTomography demonstrator, it's performance was tested in three aspects: 1) ability to produce correct energy spectra measured from the crystals, 2) ability to produce realistic count rates, and 3) ability to determine correct z-coordinates for the singles. The first two aspects tested for accurate definitions of materials and physics, while the third aspect tested the photon transport model and coordinate determination logic.

Simulation of LYSO intrinsic activity

As described in Chapter 4.1, the radioactive isotope of lutetium, ^{176}Lu, decays by β^- emission into an excited state of hafnium-176. The excitation of ^{176}Hf relaxes with a cascade of three gamma rays of 88, 202 and 307 keV. The β-particles have a high probabil-

ity to be absorbed inside the crystal whereas the de-excitation photons are more likely to escape the crystal. To detect both types of radiation, the simulation was set up so that one LYSO crystal was defined as sensitive detector, and this detector crystal was surrounded by other LYSO crystals. The experimental measurement of LYSO intrinsic activity was done by placing 4 modules close together and measuring one of the total of 20 crystals. Instead, the simulation set-up was simplified by creating one crystal with the original measures ($3\times3\times150$ mm^3) and around it 4 crystals with a size of five times that of the centre crystal.

Radioactive decay is not included in the low energy physics package, so the process was activated manually. Gamma cut was set to 1 μm in order to track characteristic x-rays. To include the radioactive decay into the crystals, separate ion sources of ^{176}Lu needed to be defined at the same locations as the crystals. The source inside the detecting crystal was the size of a real crystal with an activity of 374 Bq. The sizes of the surrounding crystals and thus the sources were set to $6\times7.5\times150$ mm^3, and the activity of each was set to 1777 Bq so that the total activity of the surrounding crystals, 7106 Bq, corresponds to nineteen $3\times3\times150$ mm^3 crystals.

The digitization was done with some differences from what was described in the beginning of this chapter. Pulse adding was done with the original hit adder module instead of the WLS processor since the locations of the hits were not of interest, and the low energy threshold was set at 40 keV in order to see all of the gamma peaks. In the simulation of intrinsic activity as well as in the following simulation for positron source detection, energy resolution was modelled using information about the efficiencies of the LYSO crystals and the MPPCs. For this purpose four digitizer modules were used: light yield for crystals' light yield, transfer efficiency for the fraction of light reaching the MPPC, intrinsic resolution blurring for the crystals' intrinsic energy resolution (at 511 keV), and quantum efficiency for the efficiency of the MPPC (at 420 nm). The used parameters are shown in Table 5.3. The output signal when using resolution modelling is the number of photoelectrons instead of energy, so the output was calibrated using an automatic calibration module that utilises the efficiency parameters. Coincidence sorting was omitted as the setup only consists of single events.

Table 5.3: Digitizer modules and parameter values used to model energy resolution of the system.

Module name	**Parameter value**
Light yield	3200 (see Table 4.1)
Transfer efficiency	0.18 (see Chapter 4.2.2)
Intrinsic resolution	0.08 (see Table 4.1)
Quantum efficiency	0.35 [32]

Simulation of positron source detection

This simulation was run with two modules placed on opposite sides of the scanner so that the scanner diameter was 10 cm. The source used in this validation simulation was a ^{22}Na point-like source covered by a Delrin (polyoxymethylene) capsule, with specifications shown in Table 5.4. The source was placed to the centre of the field of view.

Simulation for validating axial coordinate determination

The WLS firing pattern and the axial coordinate determination was studied with simulation run where two modules were placed on opposite sides with a distance of 15.4 cm. A line source was chosen for this simulation so that axial sensitivity could be studied. The source was placed in the centre of the transaxial plane in the FOV, parallel to the z-axis of the scanner. The specifications of the line source are presented in Table 5.4.

Table 5.4: Specifications of positron sources used in simulations.

	Point source	**Line source**
Isotope	^{22}Na	^{22}Na
Source size (height×diameter)	1×1 mm^2	200×1 mm^2
Capsule material	Delrin	Delrin
Capsule size (height×diameter)	25.64×6.41 mm^2	200×6 mm^2
Activity	675 kBq	1 MBq

5.2 Simulations of the performance characteristics

The simulations of performance characteristics were done according to standard NEMA NU 4-2008 that is written for testing of small animal PET scanners. It is the best choice also for other small scanners since it utilizes more appropriate sizes for sources and phantoms than the standard for clinical scanners. Using GATE to evaluate performance according to NEMA NU-4 has been validated e.g. for Inveon PET scanner [38].

Sensitivity

The sensitivity simulations were run using a back-to-back photon-pair point source, in which two 511 keV photons emitted at 180 degree angle without simulating positron decay of an ion. This eliminates the need for scatter correction by extrapolation from variable diameter phantoms and correction for ionic branching ratio. The source had an activity of 1 Mbq that is low enough for sensitivity measurements. According to the NU 4-2008 standard, the activity of the source should be kept so low that count losses and random counts are negligible. In other words, count loss should be less than 1 % and the rate of random counts should be less than 5 % of the true count rate [14].

The following scanner configurations were studied for sensitivity. Items 2 and 3 are also illustrated in Figure 5.1.

1. Configuration with 2 and 4 modules in coincidence
2. Configuration with 8 modules; 4 sectors and 2 layers
3. Configuration with 6 modules; 3 module layers in two sectors

The scanner diameter in all of the simulations was 15.4 cm. The current constructed AvanTomography demonstrator is equivalent to the configuration presented on the right side of Figure 5.1, with the exception that it has only six modules so that there are two module layers on two opposite sectors and one layer on the other two.

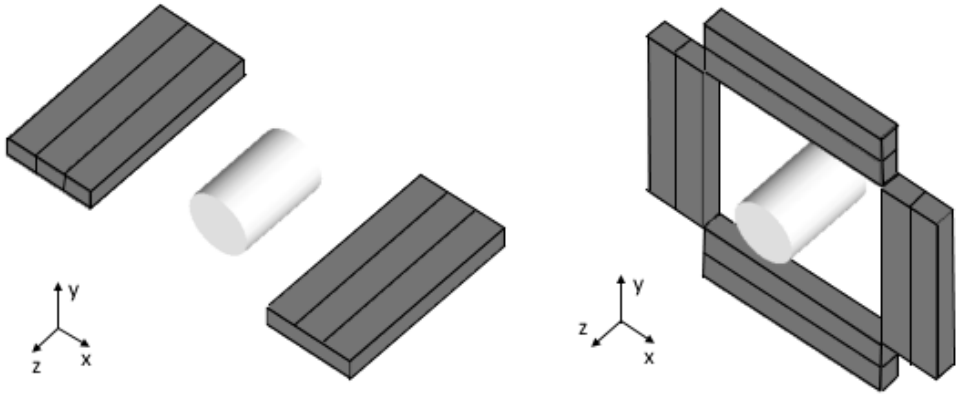

Figure 5.1: Two modelled scanner configurations with a cylindrical phantom in the field of view. Left: A configuration with two sectors and three module layers. Right: A configuration with four sectors and two layers.

Count rate and scatter fraction

Noise equivalent count rate and scatter fraction were determined for the 8-module demonstrator model, using NEMA NU 4-2008 defined rat like phantom: a solid cylinder made of polyethylene, 150 mm long and 50 mm in diameter. An ^{18}F source was placed inside the cylinder in a 150 mm long and 3.2 mm diameter water filled hole at 17.5 mm radial distance parallel to the central axis. [14] A series of simulations were run so that the total activity of the phantom was reduced from 100 MBq to 1 MBq in several steps during which short scans were simulated.

The true, random and scattered coincidences that are needed in the calculations were obtained from the GATE output data by analysing the annihilation event information and the scattering information of the coincidences. This way it was possible to get the amounts of true, random and scattered events without needing to measure these from sinograms.

6 RESULTS AND DISCUSSION

The results were analysed and plotted using a custom code based on ROOT data analysis framework [39]. In the first part of this chapter the results from model validation are shown and discussed. The second part presents the results for the performance characteristics.

6.1 Validation of the model

Energy spectra

The energy spectrum of the single events from simulation of intrinsic activity of LYSO is plotted in Figure 6.1. The spectrum shows the de-excitation γ-peaks at 202 and 307 keV from surrounding crystals; the peak at 88 keV cannot be seen because it has high internal conversion probability. The peak at 55 keV is the characteristic x-ray emission Kα line of Lutetium, which results from the photoelectric absorption of photons in the LYSO crystal. The continuous spectrum seen in the histogram comes from the β^- particles and γ photons that do not escape the crystal but release their energy within.

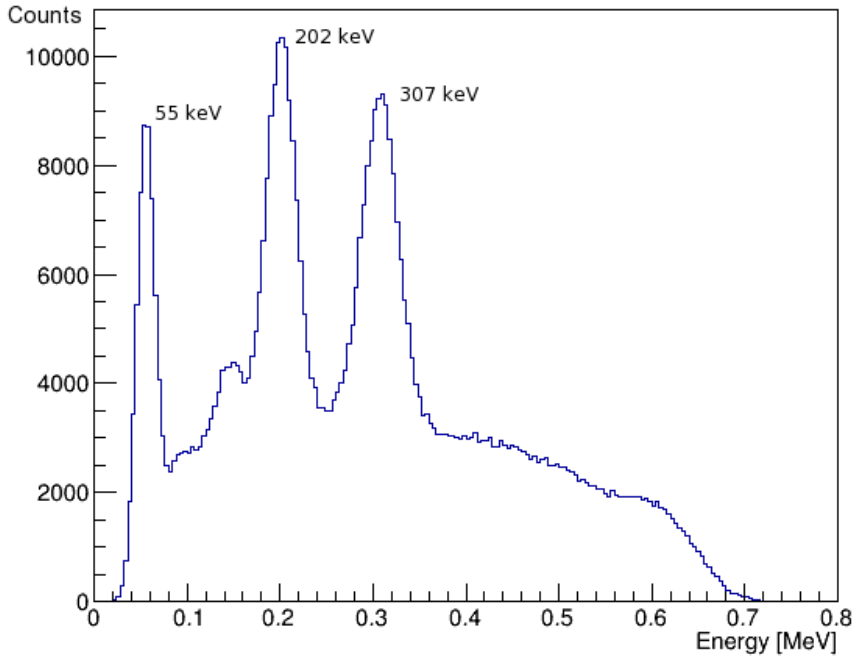

Figure 6.1: Energy spectrum of intrinsic activity of a LYSO crystal that is caused by decay of Lutetium-176. The spectrum shows de-excitation peaks at 202 and 307 keV, characteristic x-ray peak at 55 keV and the continuous radiation from β-particles and scatter.

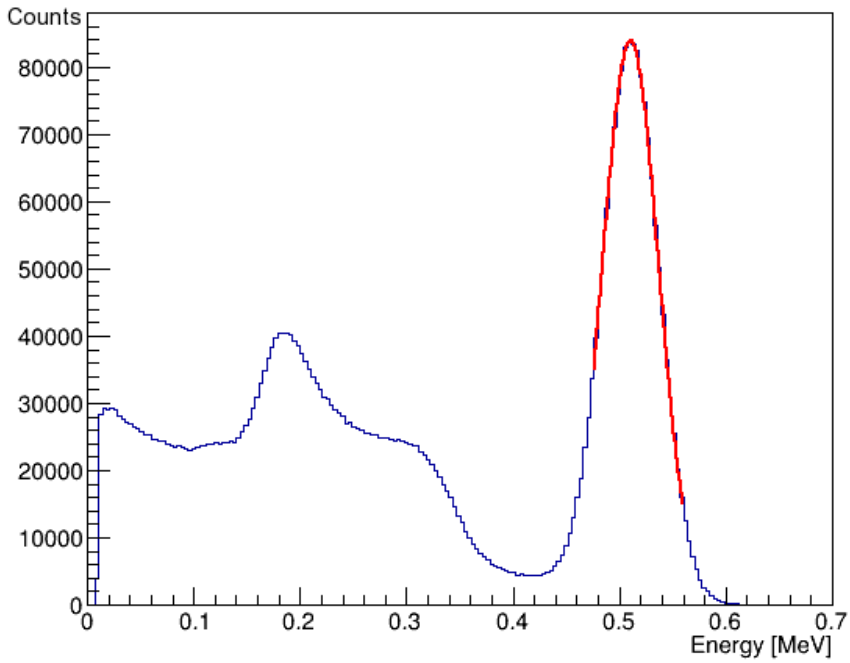

Figure 6.2: The energy spectrum of a crystal when a 675 kBq ^{22}Na source is placed in the field of view. The peak at 511 keV is fitted with a Gaussian curve for which σ=27.6 keV.

Figure 6.2 shows the energy spectrum histogram of single events from the simulation run with a positron emitting source. The spectrum has a peak at 511 keV as expected, while the events at lower energies consist of scatter, de-excitation γ-rays and characteristic x-rays of the materials. Both spectra were visually compared to experimental results obtained from the earlier version [31], and a good agreement was found. The level of low energy counts (below 200 keV) in positron source measurement was lower in the simulations than in the experimental results, but this is likely due to noise which is not included in the simulations.

What can be seen in both intrinsic and positron detection energy spectrum results is that the low-level energy threshold is of major importance when using a scanner with Lutetium-based crystals. To avoid the intrinsic peaks affecting the NECR, the threshold has to be set above 307 keV, accounting also for energy resolution. Yamatomo et al. recommend a threshold of at least 350 keV [40]. However, in preclinical scanners improving sensitivity is even more important than avoiding the random counts that result from accepted intrinsic counts, thus sometimes a considerably lower threshold is used. Goertzen et al. studied a collection of preclinical PETs with LYSO or LSO crystals using the NEMA NU 4-2008 standard, for which the low energy thresholds range from 100 keV (Sedecal VrPET system) to 385 keV (Philips Mosaic HP) [41]. When VrPET system was studied by Lage et al. the sensitivity was seen to increase 140 % when the threshold was lowered from 400 to 100 keV [42]. On the other hand, a low threshold increases the fraction of lower energy scattered counts that add noise to the image, de-

grading the quality. In case the image quality is more important than sensitivity as might be in clinical scanners, it is desirable to include only the photopeak counts. The width of the energy window is, however, limited by the energy resolution of the system, as the energy reading is blurred by the properties of the crystals and photon detectors. Based on these results, an energy window of 350 to 650 keV was chosen for the rest of the simulations.

The energy resolution of the system was extracted from the energy spectrum of the simulation with a positron source. As explained in Chapter 2.1.5, the energy resolution is defined as the FWHM of the 511 keV peak, thus:

$$R_E = \frac{FWHM}{E_{peak}} = \frac{2\sqrt{(2\,ln2)}\sigma}{E_{peak}} \tag{6.1}$$

A Gaussian fit on the peak gave standard deviation (σ) of 27.60 keV when E_{peak} was 511 keV, which results in energy resolution (R_E) of 12.7 %. The energy resolution obtained from the measurements done with the AvanTomography demonstrator was 14 %. The simulated energy resolution is certainly the ideal value that is not achievable in practise, so it was expected that the real resolution is higher. As the energy resolution depends on the properties of the crystals (intrinsic $R_{E,}$ light yield and transfer efficiency) and the photon detectors (quantum efficiency), the energy resolution varies over different scanners. Also there is some variation between individual crystals of a scanner, so resolution is given as the average value. Some examples for scanners with lutetium-based scintillators are 19 % in the microPET [43], and 25 % and 26 % in LabPET4 and LabPET5 [44]. The simulated resolution value was used in the rest of the simulations as Gaussian energy blurring to avoid the more detailed modelling and increase simulation speed.

Single count rates

Single event rate was calculated from the simulations of intrinsic activity and positron source for singles within an energy window [350, 650] keV. The count rates are collected into Table 6.1. The simulated count rates are to be compared with experimental measurements when the second version of the prototype that this model is based on is fully functional.

Table 6.1: The rates of single events within range of 350 keV to 650 keV obtained from the simulations. The activity of the ^{22}Na source was 675 kBq.

	Single count rate
LYSO intrinsic activity	180 cps
^{22}Na source	8,800 cps

The simulation with a positron source did not include the intrinsic radioactivity of LYSO, but a simple summation gives the total rate of energy filtered singles to be close

to 9 kcps. The level of intrinsic counts is likely the same in a regular module set up as in the cluster of four modules as in the simulation because at energies higher than 350 keV the counts result from β^- particles emitted inside the same crystal. At low source activity the amount of singles from intrinsic activity of the crystals can be considerable related to the rate of source-associated singles, and must be taken into account, although the relative amount of intrinsic events might not be as high after coincidence sorting. It might be advisable to add intrinsic activity to simulations of the system, but a realistic source simulations of ^{176}Lu would slow down simulation speed considerably. A better option would be to add the obtained single event rate as noise at the considered energy level.

WLS model validation results

The spread of scintillation light inside crystals causes the WLS strips to be fired in clusters. The size of the clusters is of interest because it affects the resolution that can be achieved in the axial direction, which is why the distribution of cluster sizes was studied. The results for energy-gated singles are shown in a histogram in Figure 6.3.

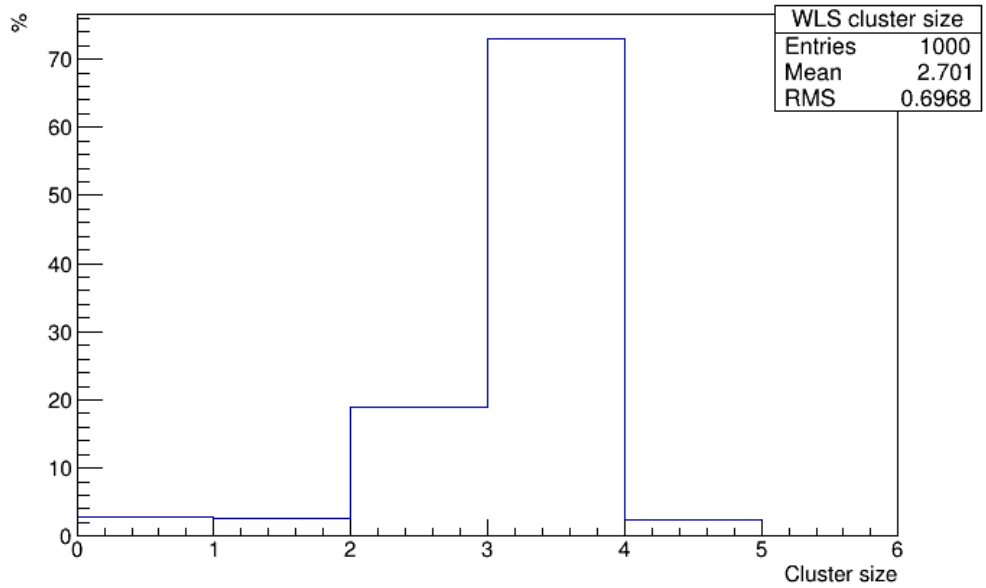

Figure 6.3: WLS strip cluster sizes for [350, 650] keV singles. Clusters of 3 strips make 73 % of all clusters, while the mean size of clusters is 2.7. Singles with clusters of 0 or 1 strip are discarded before coincidence sorting.

From the histogram it can be seen that cluster size 3 has the highest occurrence, while cluster sizes 0, 1 and 2, and more than 3 have considerably lower occurrence. A closer look at the data reveals that most clusters smaller than 3 strips occur close to the ends of the crystals. This can be explained by the small gap at both ends of crystals that are not covered by strips. For this reason discarding singles with clusters of size 1 can be justified; in case the single was at a crystal end the correct cluster size could be 3 for these events, causing the axial coordinate to distort 3 mm towards the centre. For cluster size

2, however, not all the singles were at crystal ends. In some cases the hit was so close to the middle of two strips that only two WLS strips fired, and the cluster size is therefore correct. Thus discarding clusters of size 2 would result in losing a considerable amount of data. Cluster sizes 4 and 5 on the other hand only happen if the annihilation photon scattered inside the crystal depositing energy at least twice.

Figure 6.4 shows the axial coordinates of singles that compose the detected coincidences of the model with two modules. The used z-coordinate determination method causes the discrete axial positions. From this plot and the cluster size histogram it can be concluded that determining the z-coordinate to the centre of a strip rather than to the middle of two strips is much more likely. The high peaks at -66 mm and 66 mm arise from distortion of the z-coordinate at the edges of the axial FOV; the size 3 clusters at the edges are mistaken for size 2 clusters due to lack of strips and both types of events are piled up at the same position. Figure 6.5 shows the axial sensitivity profile of the system which exhibits the typical shape of a 3D scan with a peak at the centre of the axial FOV [45].

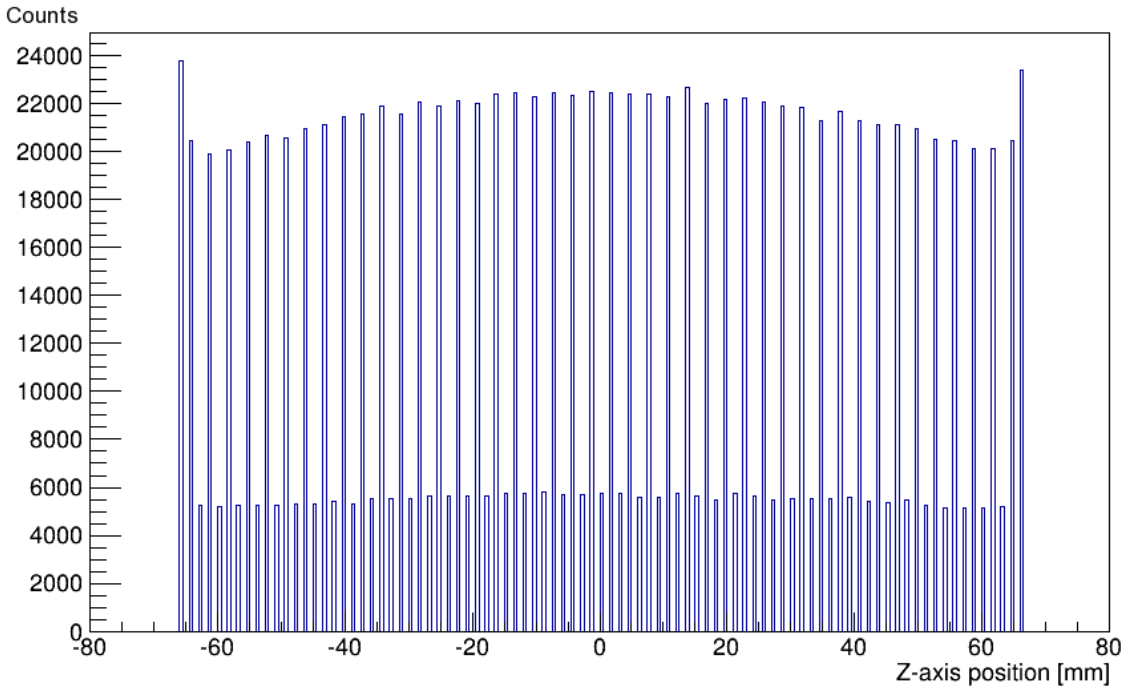

Figure 6.4: The axial coordinates of single events composing the coincidences from a scan of a line source. The high occurrence of size 3 clusters over size 2 clusters result in more of the coordinates to be discretised to middle of strip z-coordinates.

The clustering results could not be validated against measurements because the current electronic processing of WLS signals does not support this method of z-coordinate determination. Instead the system only saves the index of the WLS strip from which a signal is first obtained. This is likely to be the strip in which the signal path from the site of scintillation light absorption and re-emission to the strips MPPC is the shortest. The first

strips to give a signal might not be the middle most strip but, for a size 3 cluster, one of the strips on the sides.

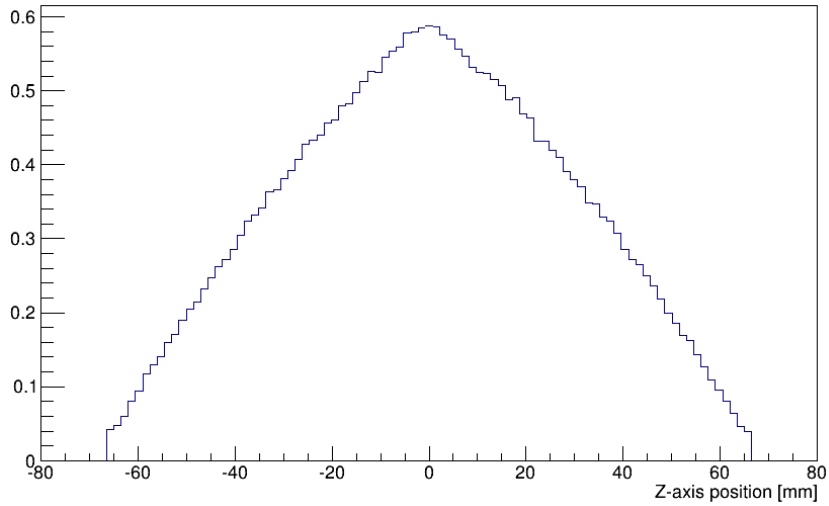

Figure 6.5: Axial sensitivity profile of the system with two axially oriented modules. The profile has the typical peak shape of a 3D scan. The y-axis of the figure shows the relative sensitivity.

In addition to these methods, a third option is to save the amplitudes of the signals obtained from fired strips. Saving the amplitudes can be used to construct a continuous z-coordinate that yields a better resolution than the discrete method, as was done in the AX-PET scanner [19].

Determining the simulated spatial resolution was not included in this thesis work, but the results of the WLS signal processing of the constructed model show that it is capable of reproducing realistic resolution of the system. The model could be used to produce list mode or sinogram data that is reconstructed into images from which the spatial resolution is determined. However, what can be seen from the z-positioning of single events is that the axial resolution is not strictly comparable to a system with an axial pixel size of 1.5 mm, since the distribution over the axis is not even but every other coordinate has a higher probability to be chosen. This also raises a question about the optimal number and pitch of the strips.

6.2 Performance characteristics

Sensitivity

The scanner's sensitivity from each simulation was calculated using Equation 2.4. The sensitivities were calculated for total system sensitivity, excluding calculations of sensitivities for each image slice. The results for the first and second simulation set ups (see Chapter 5.2) are shown in Table 6.2. Considering just the geometric configuration of the system with 2 and 4 modules, the doubling of sensitivity is well established, as the

covered solid angle is doubled. From 4-module to 8-module configuration, sensitivity is more than doubled. This layering effect was further studied in the third simulation set up, the results of which are presented in Table 6.3. The result for sensitivity is highly dependent on the solid angle coverage of the scanner, i.e. the scanner diameter and axial FOV. This is why the values for sensitivity that were obtained for the studied configurations cannot be compared to full sized preclinical or organ dedicated PET scanners. In the potential commercial scanner constructed based on AvanTomography demonstrator, the number of modules would likely be more than eight, depending on the application, so the sensitivity of a complete scanner would be higher. As the diameter of the potential full scanner could also to be other than 15.4 cm, further study on the sensitivity is necessary when the configuration is defined.

Table 6.2: Sensitivities for the model with two, four and eight modules (two layers in 4 sectors) in serial configuration. See chapter 5.2 for reference of configuration.

	Two modules	**Four modules**	**Eight modules**
Sensitivity	0.497 cps/kBq	0.993 cps/kBq	2.211 cps/kBq

Table 6.3: Sensitivities for the model with one, two and three layers. Also the percents of coincidence forming single events detected on each layer of a three-layer systems are presented.

	One layer	**Two layers**	**Three layers**
Total sensitivity	0.497 cps/kBq	1.11 cps/kBq	1.53 cps/kBq
	On first layer	**On second layer**	**On third layer**
Percent of total counts	54.5 %	30.0 %	15.5 %

The results in Table 6.3 are also presented in Figures 6.6 and 6.7 on the following page. From these results it can be seen that the second layer of modules increases the system sensitivity by 120 %, while the increase from the addition of a third layer is about 50 %. Such a large increase is possible due to coincidences forming not only between same layer modules, but also across layers, e.g. when a pair of photons hits the first layer module on one side of the scanner and a second layer module on the other. Using a logarithmic fit on the data the sensitivity of the system with four module layers can be estimated at 1.79 cps/kBq, the performance increased by 17 % compared to a three-layer system.

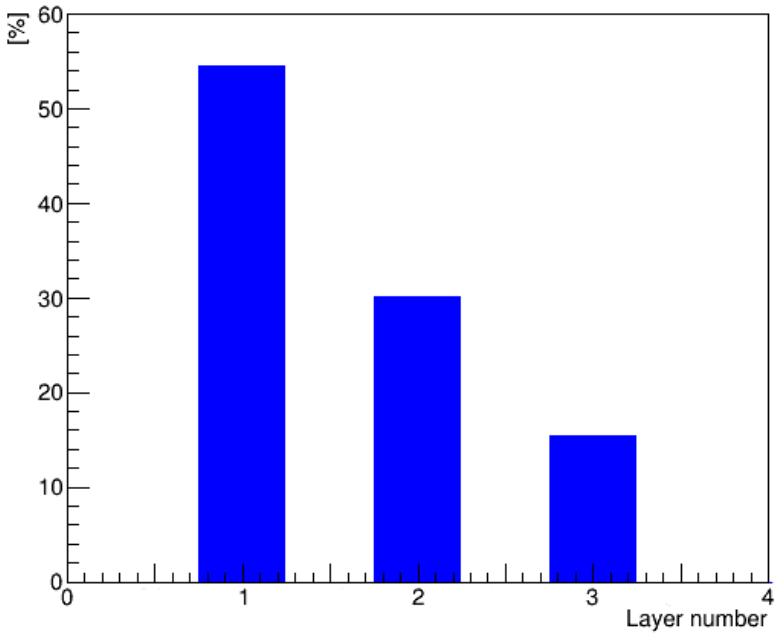

Figure 6.6: Percent of total number of coincidences detected on each module layer of a three-layer scanner. Less events are detected on layers two and three due to attenuation.

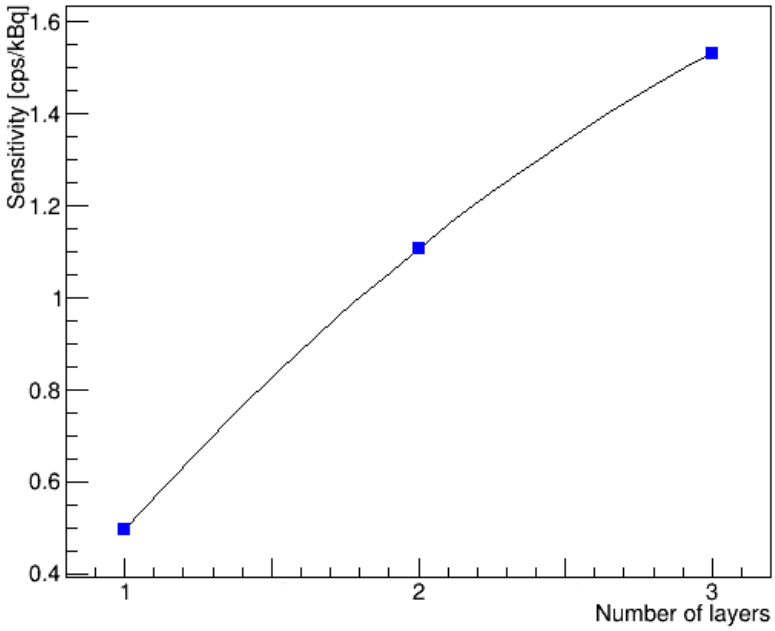

Figure 6.7: The sensitivity of the system with 1, 2 and 3 layers of modules. Sensitivity is increased by 120 % when a second layer is added, and 50 % when a third layer is added. The increase stabilises with more layers added.

It is possible to improve the system's sensitivity by adding layers of modules up to the number at which the sensitivity increase curve stabilises. Thus, in order to get the best performance, this number of layers should be used. In practise, adding layers will also increase the size and the cost of the system, so the optimal number of layers might not be the same as the number giving the best sensitivity. These results show that adding a second layer is definitely expedient; the second layer is actually more cost-effective than the first. Adding a third layer is more debatable, though its benefit on sensitivity is still apparent.

The theoretical crystal depth of one module is 5 mm (3 mm + 2/3*3 mm). The crystal depth of two module layers, 10 mm, corresponds to many current small PET detectors [41], while full body PET scanners generally have longer crystals to achieve a higher probability of stopping the photons [9]. As the attenuation length of LYSO is 1.2 cm, based on Equation 2.3, 10 mm of LYSO is able to stop 58 % of the photon flux, while three module layers would stop 72 %. The axial construction of AvanTomography allows increasing the effective crystal depth by adding layers without spatial resolution loss, but this benefit is limited by packing density of the modules; the further the crystals are from the centre of the FOV the less counts they detect as they cover smaller solid angle. Thus, if the space between the layers of crystals within and between modules could be reduced, an increase in sensitivity would also be seen.

Scatter fraction

The obtained scatter fraction of the system for a rat like phantom is 29 %, when scatter in the phantom, field of view, and the module structures are considered. The amount of scatter depends on a number of factors, most importantly the phantom, and also the used energy window and the scanner structure. Scatter increases with the size of the phantom as more photons interact with it, and a wider energy window accepts a larger percentage of the lower energy scattered photons. Yang and Cherry have shown that for a rat like phantom, scatter fraction originating from the phantom ranges from 10 to 35 %, from narrow to wide energy windows, respectively, while rest of the scatter originates from the detector and the environment [46]. This is consistent with our results; the scatter fraction for the phantom is 24.5 %, while the rest originates from the module structures other than the detector crystals. As the model does not include gantry or environment structures, scatter from other sources is not included in the scatter fraction value, so the real value is likely a bit higher. The scatter from the detector (inter-crystal scatter) is more difficult to estimate from the data only without image reconstruction, and thus is not included in the scatter fraction, but the amount of detector scatter can also be significant. The amount of detector scatter is lowest for single-layer block detectors and higher for other detector designs [41]. The layered structure of AvanTomography is likely to produce high amount of detector scatter. The amount of inter-crystal scatter in the AX-PET detector was about 20 %, as its readout is specifically designed for collect-

ing the scattered counts [21]. The readout in the current design of AvanTomography is different and it is not intended for collecting inter-crystal scatter information as the development is in an early phase and no scatter corrections have been tested. Therefore the amount of detector scatter in the accepted events should be lower than in AX-PET. The simulation data shows that about 50 % of photons undergo Compton scattering in the detector, although a major part of this is intra-crystal scatter that does not affect image quality. If inter-crystal scatter was estimated to be ~10 %, the total scatter fraction would be as high as 40 %, which is substantial compared to commercial small animal scanners studied by Goertzen et al. for which the scatter fractions range from 12.7 to 34.4 % [41].

Noise equivalent count rate

The noise equivalent count rates were calculated from the coincidence data of the simulation with a rat sized phantom using Equation 2.8. The obtained NECR values for each simulation run were plotted against the total activity, presented in Figure 6.8, and the peak NECR and NECR at 10 MBq are summed in Table 6.4. The NECR is highly dependent on the used phantom and so depends on the application (e.g. small animal, organ specific, total body) of the scanner. The NECR of a system depends on several factors, for instance the sensitivity, scatter fraction and count losses. A typical NECR curve has an ascending region and a peak after which the dead time and random counts reduce start reducing the value. The NECRs of commercial preclinical PET scanners tested by Goertzen et al. have large variations; NECR at 10 MBq ranging between 20 and 60 kcps, and peak NECR ranging between 30 and 350 kcps at source activity of 30 to 250 MBq [41].

Table 6.4: The noise equivalent count rate for 10 MBq and the peak noise equivalent count rate for an 8-module system using a rat sized phantom.

Activity	**NECR**
10 MBq	244 cps
50 MBq	430 cps (peak)

The system's peak NECR of 430 cps was seen at 50 MBq. The peak value is considerably lower than the values for the preclinical PETs which is expected as the 8-module systems used in these simulations has a very narrow axial field of view (~12 mm) that decreases the total sensitivity. In case more rings of 8-modules were added to widen the axial FOV, it is expected that the NECR would overall improve significantly. For example, in 3D mode, the sensitivity would more than double if a second ring was added.

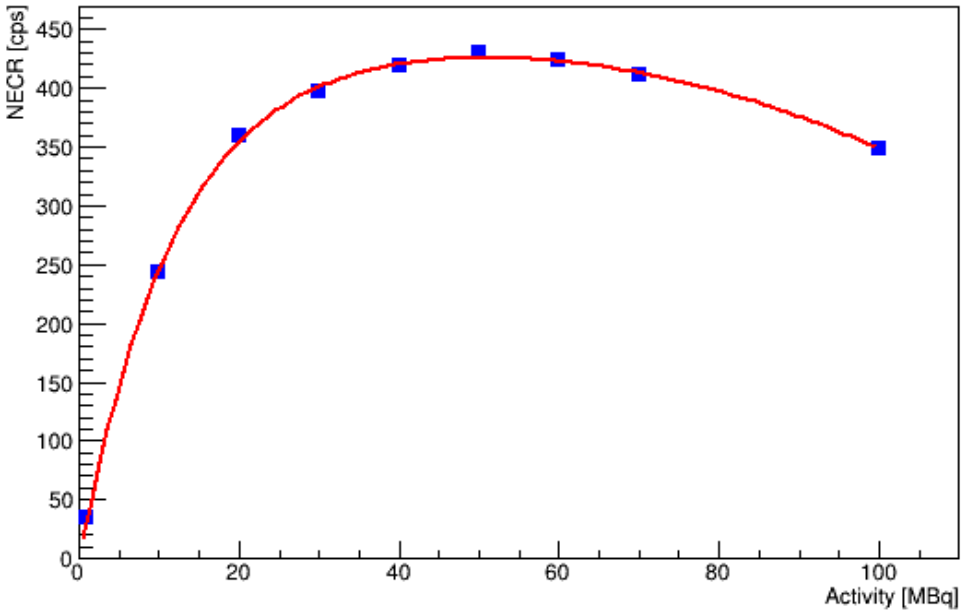

Figure 6.8: The NECR plotted against activity for an 8-module demonstrator. The peak NECR of 430 cps is reached at 50 MBq.

The source activity where the peak is reached does however fall within the range of the compared systems, as this value is mostly dependent on the dynamic performance, i.e. the dead time and the length of the coincidence window. The coincidence window used in the simulations was relatively wide, 10 ns, so if a more narrow window was chosen, the amount of random counts would be smaller, resulting in higher NECR. The modelling of dead time for the simulations was a simplification of reality; in fact reading the crystal layers with rows of WLS strips means that at high counting rates recovering the axial coordinate of single events might fail. Depending on the WLS strip readout scheme that is being used, for two pulses on the same layer but in different crystals, either only one axial coordinate is recovered (when the first to fire is chosen), or multiple clusters are saved, which might lead to failing of coordinate determination. This multiplicity effect is even more eminent if more crystals are added to a layer, so a more detailed modelling of dead time is needed especially if the modules are augmented with more crystals. Also, pile-up is not modelled independently but the pile-up time is included in the dead time, which in most cases has the same influence on the count rate, however.

7 CONCLUSIONS

This thesis describes the construction of a computer model of an axial PET demonstrator AvanTomography, and the preliminary results of Monte Carlo simulations run with the model. The model was built according to the actual demonstrator that is being constructed as part of the same project. The geometry comprises of individual modules that can be multiplied and arranged into the desired scanner configuration. Each module has five individually read scintillating crystals in two layers, and rows of WLS strips orthogonally to the crystals. In order to read the axial coordinate of the events as with the WLS strips, an efficient analytical model was used to simulate the scintillation photon transport in the crystals and strips. This model together with the coordinate determining logic was implemented into GATE as a new digitizer processing module. The existing digitizer modules were used to model the rest of the properties of the system using parameters corresponding to the real demonstrator. Sets of simulations were then run to test the model and to study the performance of the demonstrator.

First, the energy spectra and single count rates of LYSO intrinsic activity and positron source simulations were studied. The simulated energy spectrum and energy resolution at 511 keV agree with the experimental ones, resolution being 13 % compared to the experimental 14 %. The simulated count rates are reasonable; they are to be compared against experimental measurements as soon as the demonstrator is fully functional. The second set of simulations was run to study the axial coordinate determination using WLS strips. The results for clustering and coordinate distribution were expected, proving that the model is able to reproduce the axial coordinate so that it can be used to determine spatial resolution of reconstructed images and to study the optimal arrangement of the strips.

Then, the demonstrator's performance was studied with simulations to find the sensitivity, scatter fraction and noise equivalent count rate. The sensitivity of a 2-module system with a 15.4 cm diameter is 0.5 cps/kBq, and added modules increase the sensitivity as expected. It was also shown that the increase of sensitivity when a second module layer is added is 120 %, and 50 % when a third layer is added. These are significant increases indicating that at least two module layers are necessary, but a third layer would also considerably improve performance in a system that aims for high sensitivity. The scatter fraction of an 8-module system for a rat sized phantom is evaluated to be at least 29 % when the low energy threshold is set at 350 keV, and the peak noise equivalent count rate is 430 cps at 50 MBq.

Some features of the real scanner were simplified in this model to efficiently simulate the most important characteristics. In future, some of these features could be added to the model, depending on the scope. The most notable features that are lacking are the physical electronics boards and gantry that add scatter, and the modelling of intra-layer crystal multiplicity that effects the system's count rate performance. Despite these deficiencies, the results show that the model can be used in simulations of axial PET to study the performance of the system.

The geometrical configuration was designed to be flexible, allowing changes to the structure of the module and the scanner configuration be made in order to test the effects of planned changes to the configuration. Many parameters in the digitizing and coincidence sorting are not final either, and these choices affect the results, but further simulations can be run to optimise the parameters. In addition to the measures of performance that were studied in this thesis, future work with the model may include image reconstruction and measuring of spatial resolution and image quality from the reconstructions. In conclusion, the model can be used to test numerous geometrical configurations and system parameters before implementation, thus contributing to the development process of AvanTomography demonstrator.

REFERENCES

[1] Phelps, M. E., Hoffman, E. J., Mullani, N. A. & Ter-Pogossian M. M. Application of annihilation coincidence detection to transaxial reconstruction tomography. Journal of Nuclear Imaging, 1975, 16(3), pp. 210-224.

[2] Ido, T., Wan, C.-N., Casella, V., Fowler, J. S., Wolf, A. P., Reivich, M. & Kuhl, D. E. Labeled 2-deoxy-D-glucose analogs. 18F-labeled 2-deoxy-2-fluoro-D-glucose, 2-deoxy-2-fluoro-D-mannose and 14C-2-deoxy-2-fluoro-D-glucose. J Label Compd Radiopharm, 1978, 14, pp. 175–183.

[3] Maisey, M. N. Positron emission tomography in clinical medicine. In: Bailey, D. L., Townsend, D. W., Valk, P. E. & Maisey, M. N. (eds) Positron Emission Tomography. Springer, 2005, pp. 1-12.

[4] Wienhard, K., Schmand, M., Casey, M. E., Baker, K., Bao, J., Eriksson, L., et al. The ECAT HRRT: performance and first clinical application of the new high resolution research tomograph. Nuclear Science, IEEE Transactions on, 2002, 49(1), pp. 104-110.

[5] Braem, A., Chesi, E., Joram, C., Seguinot, J., Weilhammer, P., De Leo, R., et al. High precision axial coordinate readout for an axial 3-D PET detector module using a wave length shifter strip matrix. Nuclear Instruments and Methods in Physics Research Section A: Accelerators, Spectrometers, Detectors and Associated Equipment, 2007, 580(3), pp. 1513-1521.

[6] Turkheimer, F. E., Veronese, M. & Dunn, J. Experimental design and practical data analysis for positron emission tomography. Published independently, London, 2014, 107 p.

[7] Espinosa M., Jimenez, J.C., Galliker, B., Steinbach, A. & Wille, A. Radio IC for quality control in PET diagnostics. Separation Science. Feb 2015. Available: http://www.sepscience.com/Sectors/Pharma/Articles/429-/Radio-IC-for-Quality-Control-in-PET-Diagnostics

[8] Badawi, R. D. Introduction to PET physics. University of Washington, Division of Nuclear Medicine. Jan 2015. Available: http://depts.washington.edu/nucmed/IRL/pet_intro/toc.html

[9] Saha, G. B. Basics of PET imaging: physics, chemistry, and regulations. Springer, 2010, 206 p.

[10] Cherry, S. R., & Dahlbom, M. PET: physics, instrumentation, and scanners. In: Phelps, M. (ed) PET. Springer New York, 2006, 130 p.

[11] Alessio, A. M., Butterworth, E., Caldwell, J. H. & Bassingthwaighte J. B. Quantitative imaging of coronary blood flow. Nano Reviews, 2010, 1, 5110 - DOI: 10.3402/nano.v1i0.5110

[12] GATE Users Guide v7.0, OpenGATE Collaboration, website. Dec 2014. Available: http://wiki.opengatecollaboration.org/index.php/Users_Guide_V7.0

[13] Performance Measurements of Positron Emission Tomographs (PETs), National Electrical Manufacturers Association, NEMA NU 2-2012, Rosslyn, Virginia, 2012, 35 p.

[14] Performance Measurements of Small Animal Positron Emission Tomographs (PETs), National Electrical Manufacturers Association, NEMA NU 4-2008, Rosslyn, Virginia, 2008, 25 p.

[15] Budinger T. F. PET instrumentation: what are the limits? Seminars in Nuclear Medicine, 1998, Vol. 28, Iss. 3, pp. 247-267.

[16] Shimizu, K., Ohmura, T., Watanabe, M., Uchida, H. & Yamashita, T. Development of 3-D detector system for positron CT. IEEE Transactions on Nuclear Science. Vol. 35, No. 1, 1988, pp. 717-720.

[17] Braem, A., Chamizo, M., Chesi, E., Colonna, N., Cusanno, F., De Leo, R., et al. Novel design of a parallax free Compton enhanced PET scanner. Nuclear Instruments and Methods in Physics Research Section A: Accelerators, Spectrometers, Detectors and Associated Equipment, 2005, 525(1), pp. 268-274.

[18] AX-PET collaboration, website. Dec 2014. Available: https://twiki.cern.ch/twiki/bin/view/AXIALPET/WebHome

[19] Beltrame, P., Bolle, E., Braem, A., Casella, C., Chesi, E., Clinthorne, N., et al. The AX-PET demonstrator—Design, construction and characterization. Nuclear Instruments and Methods in Physics Research Section A: Accelerators, Spectrometers, Detectors and Associated Equipment, 2011, 654(1), pp. 546-559.

[20] Beltrame, P., Bolle, E., Braem, A., Casella, C., Chesi, E., Clinthorne, N., et al. AX-PET: Concept, proof of principle and first results with phantoms. In Nuclear Science Symposium Conference Record (NSS/MIC), 2010, IEEE, pp. 2754-2757

[21] Gillam, J. E., Solevi, P., Oliver, J. F., Casella, C., Heller, M., Joram, C., & Rafecas, M. Sensitivity recovery for the AX-PET prototype using inter-crystal scattering events. Physics in medicine and biology, 2014, 59(15), pp. 4065-4083.

[22] Harrison, R. L. Simulation of medical imaging systems: emission and transmission tomography. In: Grupen, C., Buvat, I. (eds) Handbook of Particle Detection and Imaging. Springer Berlin Heidelberg, 2012, pp. 1095-1124

[23] Matsumoto, M., & Nishimura, T. Mersenne twister: a 623-dimensionally equidistributed uniform pseudo-random number generator. ACM Transactions on Modeling and Computer Simulation, 1998, 8(1), pp. 3-30.

[24] Ljungberg, M. Introduction to the Monte Carlo method. In: Ljungberg, M., Strand, S-E., King, M. A. (eds) Monte Carlo calculations in nuclear medicine. Institute of Physics, Bristol, 1998, pp. 1-16.

[25] Berger, M. J., Hubbell, J. H., Seltzer, S. M., Chang, J., Coursey, J. S., Sukumar, R., Zucker, D. S. & Olsen, K. XCOM: photon cross sections database. NIST Standard reference database, 1998, 8(1), pp. 3587-3597.

[26] Agostinelli, S., Allison, J., Amako, K. A., Apostolakis, J., Araujo, H., Arce, P., et al. GEANT4—a simulation toolkit. Nuclear instruments and methods in physics research section A: Accelerators, Spectrometers, Detectors and Associated Equipment, 2003, 506(3), pp. 250-303.

[27] Geant4 simulation toolkit, Geant4 Collaboration, website. Dec 2014. Available: http://geant4.cern.ch/

[28] GATE simulation toolkit, The OpenGATE Collaboration, website. Dec 2014. Available: http://www.opengatecollaboration.org/home

[29] Jan, S., Santin, G., Strul, D., Staelens, S., Assié, K., Autret, D., Avner, S., et al. GATE: a simulation toolkit for PET and SPECT. Phys. Med. Biol. 49, 2004 pp. 4543-4561.

[30] Kerhoas-Cavata, S., & Guez, D. Modeling electronic processing in GATE. Nuclear Instruments and Methods in Physics Research Section A: Accelerators, Spectrometers, Detectors and Associated Equipment, 2006, 569(2), pp. 330-334.

[31] Zedda T. Construction and testing of a positron emission tomography demonstrator (MSc thesis). Department of Signal Processing, Tampere Univesity of Technology, 2013, 47 p.

[32] MPPC Multi-pixel photon counter, S12572-025, -050, -100C/P, Hamamatsu, Dec 2014. Available: http://www.hamamatsu.com/

[33] PreLude420 Data Sheet, Saint-Gobain, Dec 2014. Available: http://www.crystals.saint-gobain.com/PreLude_420_Scintillator.aspx

[34] EJ-260 Plastic Scintillator Data Sheet, Eljen Technology, Dec 2014. Available: http://www.eljentechnology.com/index.php/products/plastic-scintillators/70-ej-260

[35] Solevi, P., Oliver, J. F., Gillam, J. E., Bolle, E., Casella, C., Chesi, E., et al. A Monte-Carlo based model of the AX-PET demonstrator and its experimental validation. Physics in medicine and biology, 2003, 58(16), pp. 5495-5510.

[36] Moradi, S. Front-end data processing of a new positron emission tomography demonstrator (MSc thesis). Department of Signal Processing, Tampere Univesity of Technology, 2013, 62 p.

[37] Baro, J., Sempau, J., Fernández-Varea, J. M., & Salvat, F. PENELOPE: an algorithm for Monte Carlo simulation of the penetration and energy loss of electrons and positrons in matter. Nuclear Instruments and Methods in Physics Research Section B: Beam Interactions with Materials and Atoms, 1995, 100(1), pp. 31-46.

[38] Lu, L., Karakatsanis, N., Ma, J., Bian, Z., Han, Y., Tang, J., Rahmin, A. & Chen, W. Performance evaluation of the Inveon PET Scanner using GATE based on the NEMA NU-4 Standards. In Nuclear Science Symposium and Medical Imaging Conference (NSS/MIC), 2013 IEEE pp. 1-4.

[39] Brun, R. & Rademakers, F. ROOT—An Object Oriented Data Analysis Framework, Proceedings AIHENP'96 Workshop, Lausanne, Sep. 1996, Nucl. Inst. & Meth. in Phys. Res. A, 1997, 389, pp. 81-86. See also http://root.cern.ch

[40] Yamamoto, S., Horii, H., Hurutani, M., Matsumoto, K., & Senda, M. Investigation of single, random, and true counts from natural radioactivity in LSO-based clinical PET. Annals of nuclear medicine, 2005, 19(2), pp. 109-114.

[41] Goertzen, A. L., Bao, Q., Bergeron, M., Blankemeyer, E., Blinder, S., Cañadas, M., et al. NEMA NU 4-2008 comparison of preclinical PET imaging systems. Journal of Nuclear Medicine, 2012, 53(8), pp. 1300-1309.

[42] Lage, E., Vaquero, J. J., Sisniega, A., España, S., Tapias, G., Abella, M., et al. Design and performance evaluation of a coplanar multimodality scanner for rodent imaging. Physics in medicine and biology, 2009, 54(18), p. 5427.

[43] Chatziioannou, A. F., Cherry, S. R., Shao, Y., Silverman, R. W., Meadors, K., Farquhar, T. H., Pedarsani, M. & Phelps, M. E. Performance evaluation of microPET: a high-resolution lutetium oxyorthosilicate PET scanner for animal imaging. Journal of Nuclear Medicine, 1999, 40(7), pp. 1164-1175.

[44] Bergeron, M., Cadorette, J., Beaudoin, J. F., Lepage, M. D., Robert, G., Selivanov, V., et al. Performance evaluation of the LabPET APD-based digital PET scanner. Nuclear Science, IEEE Transactions on, 2009, 56(1), pp. 10-16.

[45] Bailey, D. L. Data acquisition and performance characterization in PET. In: Bailey, D. L., Townsend, D. W., Valk, P. E. & Maisey, M. N. (eds) Positron Emission Tomography. Springer, 2005, pp. 41-62.

[46] Yang, Y., & Cherry, S. R. Observations regarding scatter fraction and NEC measurements for small animal PET. IEEE Transactions on Nuclear Science, 2006, 53(1), pp. 127- 132.